A Measurement of WZ Production Cross-Section Using Multivariate Analysis in $p\bar{p}$ Collisions

(陽子反陽子衝突における多変量解析を用いたWZの生成断面積の測定)

理学研究科

数物系専攻

山本　将士

Acknowledgements

I would like to thank everyone who have supported me for about two years.

I would like to thank Prof. Toru Okusawa, Prof. Yoshihiro Seiya, Prof. Kazuhiro Yamamoto and Dr.Takayuki Wakisaka for their invaluable help and advice during my study, and for their encouragement.

Contents

1 Gauge Theory

1.1 $U(1)$ Gauge theory Electromagnetic Field

We have the free-field Lagrangian,

$$\mathcal{L}_{\text{free}} = \bar{\psi}(x)(i\gamma^{\mu}\partial_{\mu} - m)\psi(x). \tag{1.1}$$

Where Dirac field undergo a local phase transformation.

$$\begin{cases} \psi(x) \rightarrow \psi'(x) = \psi(x)e^{-iqf(x)} \\ \bar{\psi}(x) \rightarrow \bar{\psi}'(x) = \bar{\psi}(x)e^{iqf(x)} \end{cases} \tag{1.2}$$

If $\psi'(x)$ is substitute in the free Lagrangian density, the Lagrangian density become the following but it is not gauge invariant.

$$\mathcal{L}_{\text{free}} \rightarrow \mathcal{L}'_{\text{free}} = \mathcal{L} + q\bar{\psi}(x)\gamma^{\mu}\psi(x)\partial_{\mu}f(x) \tag{1.3}$$

We replace the ordinary derivative ∂_{μ} by the covariant derivative D_{μ} and

$$D_{\mu}\psi(x) = [\partial_{\mu} + iqA_{\mu}(x)]\psi(x) \tag{1.4}$$

perform gauge transformation of the electromagnetic field. where $f(x)$ is a arbitrary function.

$$A_{\mu}(x) \rightarrow A'_{\mu}(x) = A_{\mu}(x) + \partial_{\mu}f(x) \tag{1.5}$$

Invariance of the Lagrangian could be achieved by associating with the matter field and gauge field. Then invariant Lagrangian is the following and in the right handed second term is the interaction between charged particles (matter field) and gauge field.

$$\begin{aligned} \mathcal{L} &= \bar{\psi}(x)(i\gamma_{\mu}D_{\mu} - m)\psi(x) \\ &= \mathcal{L}_{\text{free}} - q\bar{\psi}(x)\gamma^{\mu}\psi(x)A_{\mu}(x) \end{aligned} \tag{1.6}$$

1.2 $SU(2) \times U(1)$ Gauge theory

$$\mathcal{L}_{\text{free}} = i\left[\bar{\psi}_l(x)\gamma^{\mu}\partial_{\mu}\psi_l(x) + \bar{\psi}_{\nu_l}(x)\gamma^{\mu}\partial_{\mu}\psi_{\nu_l}(x)\right] \tag{1.7}$$

$$\left.\begin{aligned} \psi_L(x) &= P_L\psi(x) \\ \psi_R(x) &= P_R\psi(x) \end{aligned}\right\} \equiv \frac{1}{2}(1+\gamma_5)\psi(x) \tag{1.8}$$

$$\begin{aligned} \mathcal{L}_{\text{free}} = i[&\bar{\psi}^L_l(x)\gamma^{\mu}\partial_{\mu}\psi^L_l(x) + \bar{\psi}^L_{\nu_l}(x)\gamma^{\mu}\partial_{\mu}\psi^L_{\nu_l}(x) \\ &+ \bar{\psi}^R_l(x)\gamma^{\mu}\partial_{\mu}\psi^R_l(x) + \bar{\psi}^R_{\nu_l}(x)\gamma^{\mu}\partial_{\mu}\psi^R_{\nu_l}(x)] \end{aligned} \tag{1.9}$$

combine the field into two-component field

$$\Psi_l^L(x) = \begin{bmatrix} \psi_{\nu_l}^L(x) \\ \\ \psi_l^L(x) \end{bmatrix} \tag{1.10}$$

$$\bar{\Psi}_l^L(x) = \left[\bar{\psi}_{\nu_l}^L,\, \bar{\psi}_{\nu_l}^L\right] \tag{1.11}$$

$$\mathcal{L}_{\text{free}} = i\left[\,\bar{\Psi}_l^L(x)\gamma^\mu\partial_\mu\,\Psi_l^L(x) + \psi_l^R(x)\gamma^\mu\partial_\mu\bar{\psi}_l^R(x) + \psi_{\nu_l}^R(x)\gamma^\mu\partial_\mu\bar{\psi}_{\nu_l}^R(x)\right] \tag{1.12}$$

Pauli matrix

$$\tau_1 = \begin{pmatrix} 0 & 1 \\ 1 & 0 \end{pmatrix}, \tau_2 = \begin{pmatrix} 0 & -i \\ i & 0 \end{pmatrix}, \tau_3 = \begin{pmatrix} 1 & 0 \\ 0 & -1 \end{pmatrix} \tag{1.13}$$

$$[\tau_i,\, \tau_j] = 2i\epsilon_{ijk}\tau_k \tag{1.14}$$

$$U(\alpha) \equiv \exp(i\frac{1}{2}\alpha_j\tau_j) \tag{1.15}$$

$\alpha \equiv (\alpha_1, \alpha_2, \alpha_3)$
invariance global $SU(2)$ transformation

$$\left.\begin{aligned} \Psi_l^L(x) \;&\rightarrow\; \Psi_l^{L'}(x) = U(\alpha)\,\Psi_l^L(x) \equiv \exp(i\tfrac{1}{2}\alpha_j\tau_j)\,\Psi_l^L(x) \\ \bar{\Psi}_l^L(x) \;&\rightarrow\; \bar{\Psi}_l^{L'} = \bar{\Psi}_l^L(x)U^\dagger(\alpha) \equiv \bar{\Psi}_l^L(x)\exp(-i\tfrac{1}{2}\alpha_j\tau_j) \end{aligned}\right\} \tag{1.16}$$

$$\left.\begin{aligned} \psi_l^R(x) \;&\rightarrow\; \psi_l^{R'}(x) = \psi_l^R(x), \quad \psi_{\nu_l}^R(x) \;\rightarrow\; \psi_{\nu_l}^{R'}(x) = \psi_{\nu_l}^R(x) \\ \bar{\psi}_l^R(x) \;&\rightarrow\; \bar{\psi}_l^{R'}(x) = \bar{\psi}_l^R(x), \quad \bar{\psi}_{\nu_l}^R(x) \;\rightarrow\; \bar{\psi}_{\nu_l}^{R'}(x) = \bar{\psi}_{\nu_l}^R(x) \end{aligned}\right\} \tag{1.17}$$

$$J_i^\alpha = \frac{1}{2}\,\bar{\Psi}_l^L(x)\gamma^\alpha\tau_i\,\Psi_l^L(x) \;\; (i = 1, 2, 3) \tag{1.18}$$

$$I_i^W = \int d^3x J_i^0 = \frac{1}{2}\int d^3x\,\Psi_l^{L\dagger}(x)\tau_i\,\Psi_l^L \tag{1.19}$$

weak isospin charge

$$I_3^W \mid l^-, L\rangle = -\frac{1}{2} \mid l^-, L\rangle, \quad I_3^W \mid \nu_l, L\rangle = \frac{1}{2} \mid l^-, L\rangle \tag{1.20}$$

$$I_3^W \mid l^-, R\rangle = 0, \quad I_3^W \mid \nu_l, R\rangle = 0 \tag{1.21}$$

invariance under global $U(1)$ tranceformation

$$\left.\begin{aligned} J^{\alpha}(x) &= 2[J_1^{\alpha} - iJ_2^{\alpha}(x)] = \bar{\psi}_l(x)\gamma^{\alpha}(1-\gamma_5)\psi_{\nu_l}(x) \\ J^{\alpha\dagger}(x) &= 2[J_1^{\alpha} + iJ_2^{\alpha}(x)] = \bar{\psi}_{\nu_l}(x)\gamma^{\alpha}(1-\gamma_5)\psi_l(x) \end{aligned}\right\} \tag{1.22}$$

$$J_3^{\alpha} = \frac{1}{2}\,\bar{\Psi}_l^L(x)\gamma^{\alpha}\,\Psi_l^L(x) = -\frac{1}{2}[\bar{\psi}_{\nu_l}^L(x)\gamma^{\alpha}\psi_{\nu_l}^L(x) - \bar{\psi}_l^L(x)\gamma^{\alpha}\psi_l^L(x)] \tag{1.23}$$

$$s^{\alpha}(x) = -e\bar{\psi}_l(x)\gamma^{\alpha}\psi_l(x) \tag{1.24}$$

$$\begin{aligned} J_Y^{\alpha}(x) &= \frac{1}{e}s^{\alpha} - J_3^{\alpha}(x) \\ &= -\frac{1}{2}\,\bar{\Psi}_l^L(x)\gamma^{\alpha}\,\Psi_l^L(x) - \bar{\psi}_l^R(x)\gamma^{\alpha}\bar{\psi}_l^L(x)(x) \end{aligned} \tag{1.25}$$

hypercharge

$$\begin{aligned} Y &= \int d^3x J_Y^0(x) \\ &= \frac{Q}{e} - I_3^W \end{aligned} \tag{1.26}$$

$$Y \mid l^-, L\rangle = -\frac{1}{2} \mid l^-, L\rangle, \quad Y \mid \nu_l, L\rangle = -\frac{1}{2}|l^-, L\rangle \tag{1.27}$$

$$Y \mid l^-, R\rangle = - \mid l^-, R\rangle, \quad Y \mid \nu_l, R\rangle = 0 \tag{1.28}$$

$$\left.\begin{aligned} \Psi_l^L(x) &\rightarrow \Psi_l'(x) = \exp(-i\tfrac{\beta}{2})\,\Psi_l^L(x) \\ \psi_l^R(x) &\rightarrow \psi_l^{R'} = \exp(-i\beta)\psi_l^R(x) \\ \psi_{\nu_l}^R(x) &\rightarrow \psi_{\nu_l}^{R'} = \psi_{\nu_l}^R(x) \end{aligned}\right\} \tag{1.29}$$

invariance under local $SU(2)$ tranceformation

$$\left.\begin{aligned} \Psi_l^L(x) &\rightarrow \Psi_l^{L'}(x) = \exp(i\tfrac{1}{2}g\tau_j\alpha_j(x))\,\Psi_l^L(x) \\ \psi_l^R(x) &\rightarrow \psi_l^{R'} = \psi_l^R(x) \\ \psi_{\nu_l}^R(x) &\rightarrow \psi_{\nu_l}^{R'} = \psi_{\nu_l}^R(x) \end{aligned}\right\} \tag{1.30}$$

covariant derivative

$$\partial^\mu \Psi_l^L(x) \rightarrow D^\mu \Psi_l^L(x) = [\partial^\mu + i\frac{1}{2} g\tau_j W_j^\mu] \Psi_l^L(x) \tag{1.31}$$

$$\mathcal{L}_{\text{free}} = i \left[\bar{\Psi}_l^L(x)\gamma^\mu D_\mu \Psi_l^L(x) + \psi_l^R(x)\gamma^\mu \partial_\mu \bar{\psi}_l^R(x) + \psi_{\nu_l}^R(x)\gamma^\mu \partial_\mu \bar{\psi}_{\nu_l}^R(x) \right] \tag{1.32}$$

$SU(2)$ gauge field must be transformed if Lagrangian is required of invariance.

$$W_i^\mu \rightarrow W_i^{\mu'} = W_i^\mu(x) - \partial^\mu \alpha_i(x) - g\epsilon_{ijk}\alpha_j(x) W_k^\mu(x) \tag{1.33}$$

invariance under local $U(1)$ transformation

$$\psi(x) \rightarrow \psi'(x) = \exp[ig'Y\beta(x)]\psi(x) \tag{1.34}$$

covariant derivative

$$\partial^\mu \psi(x) \rightarrow D^\mu \psi(x) = [\partial^\mu + ig'YB^\mu(x)]\psi(x) \tag{1.35}$$

$$B^\mu \rightarrow B^{\mu'} = B^\mu - \partial^\mu \beta(x) \tag{1.36}$$

$$i[\bar{\Psi}_l^L(x)\gamma^\mu D_\mu \Psi_l^L(x) + \bar{\psi}_l^R(x)\gamma^\mu D_\mu \bar{\psi}_l^R(x) + \bar{\psi}_{\nu_l}^R(x)\gamma^\mu D_\mu \psi_{\nu_l}^R(x)] \tag{1.37}$$

$$D^\mu \Psi_l^L(x) = [\partial^\mu + \frac{1}{2} ig\tau_j W_j^\mu(x) - \frac{1}{2} ig' B^\mu] \Psi_l^L(x) \tag{1.38}$$

$$D^\mu \Psi_l^L(x) = [\partial^\mu - ig' B^\mu(x)] \Psi_l^L(x) \tag{1.39}$$

$$D^\mu \psi_{\nu_l}^R(x) = \partial^\mu \psi_{\nu_l}^R(x) \tag{1.40}$$

$$\begin{aligned} \mathcal{L} &= \mathcal{L}_{\text{free}} + \mathcal{L}_{\text{int}} \\ &= i \left[\bar{\Psi}_l^L(x)\gamma^\mu \partial_\mu \Psi_l^L(x) + \psi_l^R(x)\gamma^\mu \partial_\mu \bar{\psi}_l^R(x) + \psi_{\nu_l}^R(x)\gamma^\mu \partial_\mu \bar{\psi}_{\nu_l}^R(x) \right] \\ &\quad - g J_I^\mu(x) W_{i\mu}(x) - g' J_Y^\mu(x) B_\mu(x) \end{aligned} \tag{1.41}$$

If We assume that all leptons and gauge bosons are massless like this, $U(1)$ and $SU(2)$ gauge invariance is satisfied. However this model is not renomalizable. In order to obtain that the leptons and Weak bosons is gave the mass ,and the theory is renomalizable, we have to introduce the spontaneous symmetry breaking.

1.3 Spontaneous Symmetry Breaking

The leptons Lagrangian density are add to the gauge bosons Lagrangian density ,

$$\mathcal{L} = \mathcal{L}_{\text{L}} + \mathcal{L}_{\text{B}} \tag{1.42}$$

This Lagrangian density is still exactly invariant under the $SU(2) \times U(1)$ gauge transformations. Here,We introduce the Higgs mechanism to the this Glashow model to generate masses of leptons and Weak bosons($W^\pm$ and Z^0).
First to break the gauge invariance spontaneously, We must introduce a scalar field ,a Higgs field.

1.3.1 Klein Gordon Field and $U(1)$ Gauge Field

The Klein Gordon and the $U(1)$ gauge field Lagrangian density is

$$\mathcal{L}_{\mathrm{U}} = (\partial_\mu \phi)^\dagger (\partial^\mu \phi) - V(\phi) - \frac{1}{4} F^{\mu\nu} F_{\mu\nu}. \tag{1.43}$$

where

$$\phi = \frac{1}{2}(\phi_1 + i\phi_2), \;\; V(\phi) = -\mu^2 \phi^\dagger \phi - \lambda(\phi^\dagger \phi)^2, \;\; F_{\mu\nu} = \partial_\mu A_\nu - \partial_\nu A_\mu \tag{1.44}$$

To break $U(1)$ symmetry, let $\lambda > 0$, and $\mu^2 < 0$. If the spontaneous symmetry breaking occur for $\mu^2 < 0$, the ground state is where ϕ take the finite vaccume expectation value v.

$$\phi_1 \;\rightarrow\; v + \phi_1, \;\; \phi_2 \;\rightarrow\; \phi_2 \tag{1.45}$$

so,

$$\phi = \frac{1}{\sqrt{2}}(v + \phi_1 + i\phi_2) \tag{1.46}$$

To explain the interaction between gauge field $U(1)$ and scalar field ϕ,we replace the derivative∂_μ to the covariant derivative D_μ, i.e.

covariant derivative

$$\partial_\mu \;\rightarrow\; D_\mu = [\partial_\mu - ieA_\mu(x)]. \tag{1.47}$$

$$\mathcal{L} = (D_\mu \phi)^\dagger (D^\mu \phi) - V(\phi) - \frac{1}{4} F^{\mu\nu} F_{\mu\nu} \tag{1.48}$$

After a calculation,

$$\begin{aligned} \mathcal{L} = {} & \frac{1}{2}[\partial_\mu \phi_1 \partial^\mu \phi_1 - (-2\mu^2)\phi_1^2] + \frac{(ev)^2}{2}\left(A_\mu - \frac{1}{ev}\partial_\mu \phi_2\right)\left(A^\mu - \frac{1}{ev}\partial^\mu \phi_2\right) \\ & - \frac{1}{4} F^{\mu\nu} F_{\mu\nu} + (\text{interaction}) \end{aligned} \tag{1.49}$$

where, let

$$B_\mu = A_\mu - \frac{1}{ev}\partial_\mu \phi_2, \quad F_{B\mu\nu} \equiv \partial_\mu B_\nu - \partial_\nu B_\mu = \partial_\mu A_\nu - \partial_\nu A_\mu. \tag{1.50}$$

$$\begin{aligned} \mathcal{L} = {} & \frac{1}{2}[\partial_\mu \phi_1 \partial^\mu \phi_1 - (-2\mu^2)\phi_1^2] + \frac{(ev)^2}{2} B_\mu B^\mu \\ & - \frac{1}{4} F_{B\mu\nu} F_B^{\mu\nu} + (\text{interaction}) \end{aligned} \tag{1.51}$$

From this Lagrangian density, the gauge boson mass m_B is $m_B = ev$ and the scalar boson mass m_ϕ is $m_\phi = \sqrt{-2\mu^2}$. The gauge field have acquired a mass like this,which is called Higgs mechanism. So-called, this mechanism is to do gauge fixing. If the following equation is substituted to (1.43), the equation (1.51) is obtained.

$$\left.\begin{aligned} \phi \;\rightarrow\; \phi' = \tfrac{1}{\sqrt{2}}(\phi_1 + v) = \exp(-i\tfrac{\phi_2}{v})\phi = \exp(-i\tfrac{\phi_2}{v})\phi = \tfrac{1}{\sqrt{2}}(v + \phi_1) + i\phi_2) \\ A_\mu \;\rightarrow\; B_\mu = A_\mu - \tfrac{1}{ev}\partial_\mu \phi_2 \end{aligned}\right\} \tag{1.52}$$

1.3.2 Klein Gordon Filed and $SU(2)$ Gauge Field

As we want to break the local $SU(2)$ invariance, we introduce the $SU(2)$ doublet ϕ as scalar field.

The Lagrangian density is

$$\mathcal{L}_{SU} = (\partial_\mu \phi)^\dagger (\partial^\mu \phi) - V(\phi) - \frac{1}{4} W_a^{\mu\nu} W_{a\mu\nu}. \tag{1.53}$$

$$\phi = \begin{bmatrix} \phi_1 \\ \phi_2 \end{bmatrix} = \frac{1}{\sqrt{2}} \begin{bmatrix} \frac{1}{2}(\phi_1 + i\phi_2) \\ \\ \frac{1}{2}(\phi_3 + i\phi_4) \end{bmatrix} \tag{1.54}$$

To break symmetry spontaneously, let vaccume expectation value v.

$$\left.\begin{array}{c} \phi_1 \rightarrow \phi_2, \ \phi_2 \rightarrow \phi_1 \\ \phi_3 \rightarrow v + \zeta, \ \phi_4 \rightarrow -\phi_3 \end{array}\right\} \tag{1.55}$$

That is,

$$\phi \rightarrow \phi = \begin{bmatrix} \frac{1}{2}(\phi_2 + i\phi_1) \\ \\ \frac{1}{2}(v + \zeta - i\phi_3) \end{bmatrix} \tag{1.56}$$

Similarly,We replace ∂_μ to D_μ to explain the interaction between doublet ϕ and $SU(2)$ field.

$$\partial_\mu \rightarrow D_\mu = \partial_\mu + i\frac{1}{2} g \tau^a W_{a\mu} \tag{1.57}$$

$$\begin{aligned} \mathcal{L} &= (D_\mu \phi)^\dagger (D^\mu \phi) - V(\phi) - \frac{1}{4} W_a^{\mu\nu} W_{a\mu\nu} \\ &= \frac{1}{2}\left(\partial_\mu \phi \partial^\mu \phi - 2\lambda\nu^2\phi^2 - \lambda\nu\phi^3 - \frac{1}{4}\lambda\phi^4\right) - \frac{1}{4} W_a^{\mu\nu} W_{a\mu\nu} \\ &+ \frac{1}{2}\left(\frac{gv}{2} + \frac{g\phi}{2}\right)^2 \left(W_\mu^a - \frac{1}{g}\partial_\mu \phi^a - \epsilon_{abc}\phi^b W_\mu^c\right)\left(W^{\mu a} - \frac{1}{g}\partial^\mu \phi^a - \epsilon_{abc}\phi^b W^{\mu c}\right) \end{aligned} \tag{1.58}$$

$$\left.\begin{array}{c} W_{a\mu} \rightarrow W'_{a\mu} = W_{a\mu} - \frac{1}{g}\partial_\mu \phi_a - \epsilon_{abc}\phi_b W_{c\mu} \\ W_{a\mu\nu} \rightarrow W'_{a\mu\nu} = \partial_\mu W'_\nu - \partial_\nu W'_\mu - g\epsilon_{abc} W'_{b\mu} W'_{c\nu} \end{array}\right\} \tag{1.59}$$

Gauge fixing,

$$\left.\begin{aligned}
\phi \rightarrow \phi' &= \begin{bmatrix} 0 \\ \frac{1}{2}(v+\zeta) \end{bmatrix} = \exp\left(-i\tfrac{1}{2v}\tau^a\phi_a\right)\phi \\
&= \exp\left(-i\tfrac{1}{2v}\tau^a\phi_a\right)\begin{bmatrix} \frac{1}{2}(\phi_2+i\phi_1) \\ \frac{1}{2}(v+\zeta-i\phi_3) \end{bmatrix} \\
W_{a\mu\nu} \rightarrow W'_{a\mu\nu} &= \partial_\mu W'_\nu - \partial_\nu W'_\mu - g\epsilon_{abc}W'_{b\mu}W'_{c\nu}
\end{aligned}\right\} \tag{1.60}$$

1.4 $SU(2) \times U(1)$ Gauge Theory Electroweak Field

The Weinberg-Salam model, one of the most successful quantum theories besides the original QED, is curious amalgams of weak and electromagnetic interactions. Strictly speaking, it is not a "unified field theory" of the weak and electromagnetic interactions, since we must introduce two distinct coupling constants g and g' for the $SU(2)$ and $U(1)$ interactions. Nonetheless, it represents the one of the most important extensions of QED in the past quarter century.

We begin by discussing the $SU(2)$ sector. Observationally, we must incorporate a neutral, left-handed Weyl neutrino along with a Dirac electron, which can be considered to be sum of left-handed and right-handed Weyl spinors. The left-handed fermions form an isodoublet, considering of the Weyl neutrino and electron:

$$L \equiv \begin{bmatrix} \nu_e \\ e \end{bmatrix}_L \tag{1.61}$$

while the right-handed sector consists of an isosinglet,the right-handed electron:

$$R \equiv (e)_R \tag{1.62}$$

This curious feature, that electron is split into two parts, with the left-and right-handed sectors transforming differently, is a consequence of the fact that the weak interactions violate parity and are mediate by $V-A$ interactions.

These two lepton sectors transform under $SU(2)$ in the different ways:

$$\begin{aligned} L &\rightarrow \exp\left(\tfrac{i}{2}\boldsymbol{\theta}\cdot\boldsymbol{\sigma}\right)L \\ R &\rightarrow R \end{aligned} \tag{1.63}$$

Now let us examine the transformation of these field under:

$$\begin{aligned} L &\rightarrow \exp(\tfrac{i}{2}\beta)L \\ R &\rightarrow \exp(i\beta)R \end{aligned} \tag{1.64}$$

R and L transform slightly under the $U(1)$ transformation.

The action of the Weinberg Salam model consist of three parts. $\mathcal{L}_1$ is the gauge parts; $\updownarrow_2$ is the fermionic parts; and $\mathcal{L}_3$ is scalar Higgs sector:

$$\mathcal{L} = \mathcal{L}_1 + \mathcal{L}_2 + \mathcal{L}_3 \tag{1.65}$$

where;

$$\begin{aligned}
\mathcal{L}_1 &= \frac{1}{4} W^a_{\mu\nu} W^{a\mu\nu} - \frac{1}{4} F_{\mu\nu} F^{\mu\nu} \\
\mathcal{L}_2 &= i\bar{R}\gamma^\mu D_\mu R + i\bar{L}\gamma^\mu D_\mu L \\
\mathcal{L}_3 &= D_\mu \phi^\dagger D^\mu \phi - m^2 \phi^\dagger \phi - \lambda(\phi^\dagger \phi)^2 + G_e(\bar{L}\phi R + \bar{R}\phi^\dagger L)
\end{aligned} \tag{1.66}$$

where;

$$\begin{aligned}
W^a_{\mu\nu} &= \partial_\mu W^a_\nu - \partial_\nu W^a_\mu + g f^{abc} W^b_\mu W^c_\nu \\
F_{\mu\nu} &= \partial_\mu B_\nu - \partial_\nu B_\mu \\
D_\mu R &= (\partial_\mu + i g' B_\mu) R \\
D_\mu L &= \left[\partial_\mu + \frac{i}{2} g' B_\mu - \frac{i}{2} g \sigma_i W^i_\mu \right] L \\
D_\mu \phi &= \left[\partial_\mu - \frac{i}{2} g' B_\mu - \frac{i}{2} g \sigma_i W^i_\mu \right] L
\end{aligned} \tag{1.67}$$

The scalar multiplet is a complex isodoublet given by:

$$\phi = \begin{pmatrix} \phi^+ \\ \phi^0 \end{pmatrix} \tag{1.68}$$

where the doublet has charge (1,0), which can given by $Q = T^3 + \frac{1}{2}Y$, such that $T^3 = \pm\frac{1}{2}$ and $Y = 1$

Symmetry braking is indicate by:

$$\langle \phi \rangle = \begin{pmatrix} \phi^+ \\ \phi^0 \end{pmatrix} \tag{1.69}$$

After symmetry breaking, the field W^a_μ and B_μ recombine and reemerge as the physical photon field A_μ, a neutral massive vector particle Z_μ, and a charged doublets of massive vector particles $W^\pm_\mu$:

$$\begin{aligned}
Z_\mu &= \frac{g W^3_\mu - g' B_\mu}{\sqrt{g^2 + g'^2}} \\
A_\mu &= \frac{g' W^3_\mu + g B_\mu}{\sqrt{g^2 + g'^2}} \\
W^\pm_\mu &= \frac{1}{\sqrt{2}} (W^1_\mu \pm i W^2_\mu)
\end{aligned} \tag{1.70}$$

For instance,

$$(D_\mu \psi)^\dagger (D^\mu \psi) = \frac{1}{4} \left(g^2 v^2 W^{+\mu} W^-_\mu - \frac{1}{2} v^2 (g^2 + g'^2) Z^\mu Z_\mu \right) \tag{1.71}$$

By examining the mass sector, we can get the mass of the resulting vector particles:

$$\begin{aligned} M_W &= \frac{1}{2}gv \\ M_Z &= \frac{1}{2}\sqrt{g^2+g'^2}v \end{aligned} \tag{1.72}$$

These gauge boson self-interactions are one of the most striking features of the electroweak theory. The Lagrangian of the interactions among gauge bosons is derived from $\mathcal{L}_1$. As the Lagrangian $\mathcal{L}_1^{BB}$,

$$\begin{aligned} \mathcal{L}_1^{BB} = i\frac{gg'}{\sqrt{g^2+g'^2}}[&(W_\mu^\dagger W_\nu - W_\nu^\dagger W_\mu)\partial^\mu Z^\nu \\ &+ (\partial_\mu W_\nu - \partial_\nu W_\mu)W^{\dagger\nu}Z^\mu - (\partial_\mu W_\nu^\dagger - \partial_\nu W_\mu^\dagger)W^\nu Z^\mu] \\ &+ (WWA \text{ interaction}) + \cdots \end{aligned} \tag{1.73}$$

The WZ production cross section in the standard model depend on the WWZ gauge coupling, show in the Feynman diagrams of for WZ production in $p\bar{p}$ collisions.

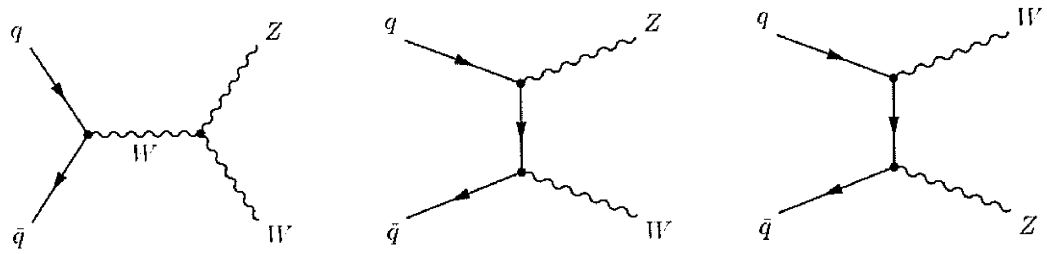

Figure 1: The t and s channel tree level Feynman diagram for WZ production.

The s channel contains that WWZ vertex that allow us to directly measure the coupling strength of the massive vector bosons to each other.

2 apparatus

The Tevatron Collider represents the high energy frontier accelerator in particle physics. The Tevatron is located at Fermilab in Batavia, Illinois USA. It is currently providing highest energy proton-antiproton with a center-of-mass energy of $\sqrt{s} = 1.96$ TeV. The collisions occur at two points in Tevatron ring which has a radius of about 1km. The collision points are instrumented with a detector in each which called The Collider Detector at Fermilab (CDF II) and DØ. This study uses data collected with the CDF II. The CDF II is a general purpose solenoidal detector which combines precision charged particle tracking, scintillator based calorimetry, and muon detection chambers and scintillators. This chapter describes the beam production and acceleration system, and the CDF II detector design.

2.1 The Accelerator Complex

The Tevatron is the last in a chain of accelerators that gradually increase the energy of protons and antiprotons. The protons are abundant and readily in nature, while antiprotons must be produced and stored. In addition, a single accelerator cannot bring particles from rest to very high energies because no magnets have the dynamic range necessary. Consideration of these requirements led to the design of a chain of accelerators at Fermilab. Figure 2 shows a diagram and aerial photograph of the Fermilab accelerator chain.

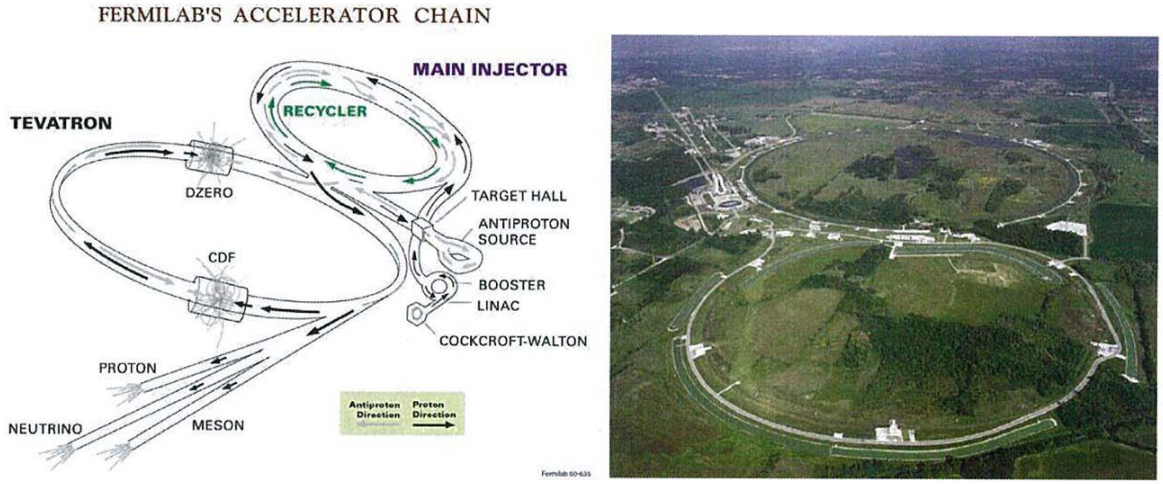

Figure 2: A diagram (left) and aerial photograph (right) of the Fermilab accelerator chain.

2.1.1 Proton Production and Boosting

The Cockcroft-Walton pre-accelerator provides the first stage of acceleration. The accelerator ionizes the hydrogen gas to H^+ ions, which are accelerated to 750 keV of kinetic energy.

The ionized hydrogen gases (H^+) enter a liner accelerator (Linac), approximately 150m long, and the ions are accelerated to 400 MeV. The acceleration in the Linac is done by a series of "kicks" from Radio Frequency (RF) cavities.

The H^+ ions with 400 MeV are injected into the Booster. The Booster is a circular synchrotron, approximately 150m in diameter. A carbon foil strips the electrons from the H^+ ions, leaving behind protons. The intensity of the protons beam is increased by injecting new protons into the same orbits as the circulating ones. The protons are accelerated from 400 MeV to 8 GeV with a series of magnets arranged around a 75m radius circle, with 18 RF cavities interspersed.

2.1.2 Main Injector

The Main Injector (MI) is a circular synchrotron seven times the circumference of the Booster and slightly more than half the circumference of the Tevatron. Main Injector has 18 accelerating cavities. It can accelerate 8 GeV protons from the Booster to either 120 GeV or 150 GeV, depending on their destination. When used to stack antiprotons, the final energy is 120 GeV. When used to inject into the Tevatron, the final beam energy is 150 GeV. As well as accepting protons from Booster, the Main Injector can accept antiprotons from the Antiproton Source. The Main Injector can accelerate beam as fast as every 2.2 seconds.

2.1.3 Antiproton Source

In order to produce antiprotons, the protons with 120 GeV are extracted from the MI and strike a nickel target at the Antiproton source. These high-energy protons striking the target produce a spray of all sorts of secondary particles. Using magnets to choose which momentum and charge we can collect 8 GeV antiprotons from this spray. Approximately one antiproton is produced per 10^5 protons. These antiprotons are directed into the Debuncher.

The Debuncher is a rounded triangular-shaped synchrotron with a mean radius of 90m. It can accept 8 GeV antiprotons from the target station, and maintain the beam at a energy of 8 GeV. Its primary purpose is to efficiently capture the high momentum spread antiprotons coming from the target using a RF manipulation called bunch rotation which reduce the antiproton momentum spread. The reduction is done to improve the Debuncher to Accumulator transfer because of the limited momentum aperture of the Accumulator at injection.

The Accumulator is also triangular-shaped synchrotron and is mounted in the same tunnel as the Debuncher. It is the storage ring for antiprotons, all of the antiprotons made are stored here at 8 GeV and cooled until need.

2.1.4 Recycler

The Recycler is an antiproton storage ring installed in the same tunnel as the MI. The proposed purpose of the Recycler was to recycle the antiproton from a Tevatron store, cooling them and storing them alongside those sent from the Antiproton Source. This was abandoned after early problems in RunII. The Recycler now accepts transfers only

from the Antiproton Source and cools them further than the antiprotons Accumulator is capable. The Recycler uses both a stochastic cooling system and an electron cooling system. Stochastic cooling is used to cool the beam in Recycler, but loses its effectiveness with higher intensities. Once above 2×10^{12} antiprotons in the Recycler, Electron cooling is required. Electron cooling works on the principle of momentum transfer between electrons and antiprotons, a highly concentrated, cool beam of electrons is driven at the same energy as the antiprotons and laid overtop of the antiprotons. The resulting glancing collisions between electrons and antiprotons transfer some of the momentum from the "hot" antiprotons to the "cool" electrons. With enough electrons, a substantial longitudinal cooling force is produced by absorbing momenta from the antiprotons allowing for more compact, brighter bunches to send to the Tevatron.

2.1.5 Tevatron

The Tevatron is the largest of the Fermilab accelerators, with a circumference of approximately 6km long. It is a circular synchrotron with eight accelerating cavities. The Tevatron can accept both protons and antiprotons from MI and accelerate them from 150 GeV to 980 GeV. In Collider mode, the Tevatron can store beam for hours at a time. Because the Tevatron is a primarily storage ring, the length of time between acceleration cycles is widely variable. The Tevatron is the cryogenically cooled accelerator. The magnets used in the Tevatron are made up of a superconducting niobium/titanium alloy that needs to be kept extremely cold (~4 K) to remain a superconductor. The benefit of having superconducting magnets is the increased magnetic fields possible when high currents can be run through thin wires without fear of damage related to excessive resistive heating.

2.1.6 Luminosity

The luminosity of collisions can be expressed as:

$$\mathcal{L} = \frac{f N_B N_p N_{\bar{p}}}{2\pi(\sigma_p^2 + \sigma_{\bar{p}}^2)} F\left(\frac{\sigma_l}{\beta^*}\right), \tag{2.1}$$

where f is the revolution frequency, N_B is the number of bunched, $N_{p(\bar{p})}$ is the number of protons (antiprotons) per bunch, and $\sigma_{p(\bar{p})}$ is the protons (antiprotons) RMS beam size at the interaction point. F is a form factor which corrects for the bunch shape and depends on the ratio of σ_l, the bunch length to β^*, the beta function, at the interaction point. The beta function is a measure of the beam width, and it is proportional to the beam's x and y extent in phase space. Table 1 shows the accelerator parameter in the current run (Run II). The current peak luminosity is $\sim 3.6 \times 10^{32}$ cm^{-2}s^{-1}. The delivered luminosity is 5.4 fb^{-1} and actual recorded luminosity is 4.5 fb^{-1}, which is collected between February 2002 and December 2008. Figure 3 shows integrated luminosity measured with CDF.

2.2 The Collider Detector at Fermilab

The CDF II detector is a general purpose solenoidal detector which combines precision charged particle tracking with fast projective calorimetry and fine grained muon detection.

Parameter	Run II
Number of bunhes (N_B)	36
Bunch length [m]	0.37
Bunch spacing [ns]	396
Protons/bunch (N_p)	2.7×10^{11}
Antiprotons/bunch ($N_{\bar{p}}$)	3.0×10^{10}
Total antiprotons	1.1×10^{12}
β^* [cm]	35
Interactions/crossing	2.3

Table 1: Accelerator parameters for Run II configurations.

Figure 3: Integrated luminosity as a function of store number between February 2002 and December 2008.

Figure 4 and Figure 5 show a cut away view and elevation view of the CDFII detector for each. Tracking systems are made up Silicon Trackers, Central Outer Tracker (COT), and Superconducting Solenoid which to measure precise trajectories and momenta of charged particles and reconstruct vertices. The solenoid surround the Silicon Trackers and COT, has 1.5m in radius and 4.8m long, and generates a 1.4 T magnetic field parallel to the beam axis. Calorimetry Systems measure the energy of particles, surround the solenoid. Muon Chambers detect the particles penetrating both Tracking Systems and Calorimetry Systems. Muons deposit small amount of ionization energy in the material because they act as minimally ionizing particles (MIP), that is, the penetrating particles are mostly muons.

2.3 Coordinate System in the CDF

The standard coordinate system to be used in the CDF is the right-handed coordinate system. The z-axis is oriented the direction of the proton beam. The x-axis points horizontally away from the detector and the y-axis is vertical pointing up-wards. It is helpful to use the cylindrical coordinate. The azimuthal angle ϕ is $x-y$ plane angle around the beam line. The polar angle θ is measured starting from the z-axis. The rapidity of a particle is defined as,

$$y \equiv \frac{1}{2}\ln\left(\frac{E+p_z}{E-p_z}\right). \tag{2.2}$$

where E is the energy of the particle and p_z is its longitudinal momentum. For highly boosted particles, $E \sim p$ and $p_z = p\cos\theta$, that is, the rapidity can be approximated by pseudorapidity,

$$\eta = -\ln\left(\tan\frac{\theta}{2}\right). \tag{2.3}$$

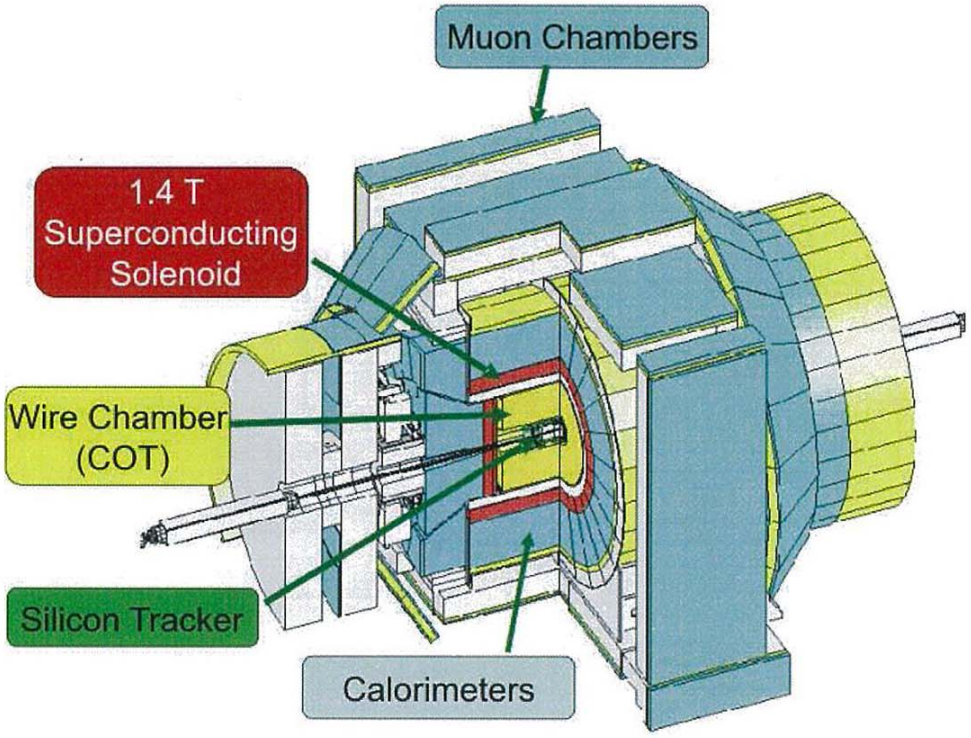

Figure 4: Cut away view of the CDF II detector.

2.4 Tracking Systems

For CDF analysis technique, precision charged particle tracking is very important. CDF II detector has an open cell drift chamber, the Central Outer Tracker (COT) covers the region $|\eta| \leq 1.0$. Inside the COT, a silicon "inner tracker" is built from three components. Layer 00 (L00) is mounted on the beam pipe, very close to the beam line. Its primary purpose is to improve the impact parameter resolution. A micro-vertex detector at very small radii, so-called Silicon Vertex Detector (SVX-II), establishes the ultimate impact parameter resolution. Two additional silicon layers at intermediate radii, so-called Intermediate Silicon Layers (ISL), provides p_T resolution and b-tagging in the forward region $1.0 \leq |\eta| \leq 2.0$, and stand-alone silicon tracking over the full region $|\eta| \leq 2.0$. The stand-alone silicon segments allow integrated tracking algorithms which maximize tracking performance over the whole region $\eta \leq 2.0$. In the central region ($\eta \leq 1.0$), the stand-alone silicon segment can be linked to the fill COT track to give excellent p_T and impact parameter resolution.

2.4.1 Layer 00

Layer 00 is installed directly in the beam pipe. L00 was added at beginning of RunII for two reasons. Firstly to improve the impact parameter resolution of the CDF detector. Placement of a minimal material silicon layer at a smaller radius provides a precise measurement. Secondly, L00 was installed to extend the useful lifetime of the silicon system. The inner layers SVX-II will have a limited lifetime due to radiation damage. The design

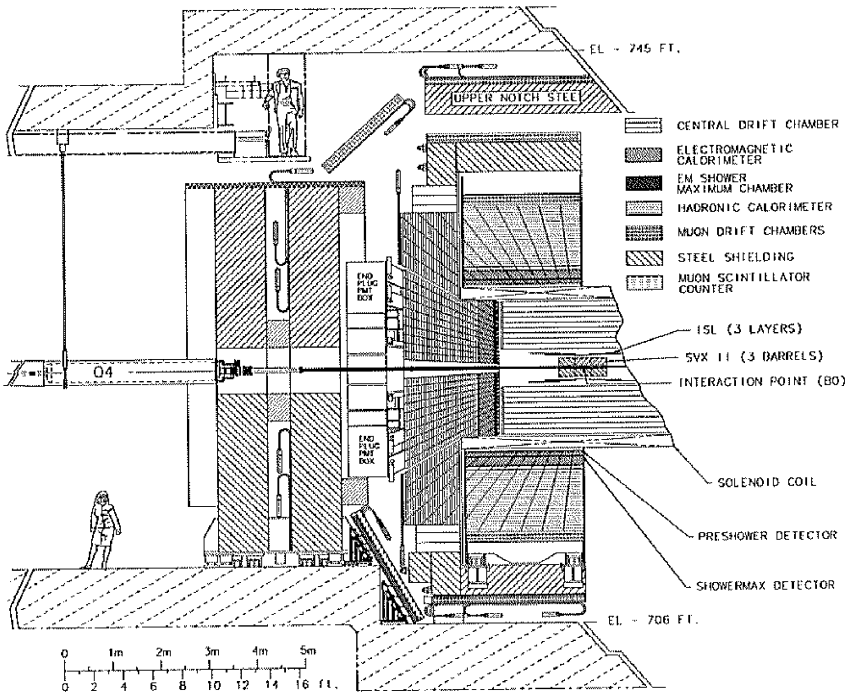

Figure 5: Elevation view of the CDF II detector.

has six narrow (128 channels) and six wide (256 channels) groups in θ at $r = 1.35$cm and $r = 1.62$cm respectively. There are six readout modules in z, with two sensors bounded together in each module for a total length of 95cm. The sensors are single-sided p-in-n silicon with a 25(50)μm implant(readout) pitch. These have been produced by Hamamatsu Photonics (HPK), SGS-Thompson (ST) and Micron. These sensors can be biased up to 500V, limited by the maximum range of the power supplies. Figure 6 shows the end view of L00 and a part of SVX-II (L0 and L1).

Figure 6: End view of Layer 00 (colored), also showing a part of SVX-II (un-colored).

2.4.2 Silicon Vertex Detector

Silicon Vertex Detector (SVX, SVX-II) is the core detector for silicon tracking and for a trigger on tracks with large impact parameter with respect to the interaction point. The SVX-II detector has 5 layers of double-sided sensors surround the L00 at radii from 2.5 to 10.6cm. Three layers (L0, L1, and L3) are made of Hamamatsu silicon with the n strips perpendicular to the p strips. The remaining two layers (L2 and L4) are Micron sensors with a stereo angle of 1.2° between the n and p strips. The strip pitch varies between 60 to 140μm, depending on the layer radius. The maximum bias voltages that can be applied to Hamamatsu and Micron sensors are 170 V and 70 V respectively, limited by the

breakdown voltage of the integrated coupling capacitors and subtle sensor effects. The SVX-II can provide track information to $|\eta| < 2.0$. Table 2 shows the design parameters of the SVX-II. Figure 7 shows 3D view and $r - \phi$ view for SVX-II.

Parameter	Layer 0 (L0)	Layer 1 (L1)	Layer 2 (L2)	Layer 3 (L3)	Layer 4 (L4)
Number of ϕ strips	256	384	640	768	896
Number of z strips	512	576	640	512	896
stereo angle (degree)	90	90	+1.2	90	−1.2
ϕ strip pitch [μm]	60	62	60	60	65
z strip pitch [μm]	141	125.5	60	141	65
Total width [mm]	171.140	25.594	40.300	47.860	60.170
Total length [mm]	74.3	74.3	74.3	74.3	74.3
Active width [mm]	15.300	23.746	38.340	46.020	58.175
Active length [mm]	72.43	72.43	72.38	72.43	72.38
Number of sensors	144	144	144	144	144

Table 2: Design parameters of the Silicon Vertex Detector.

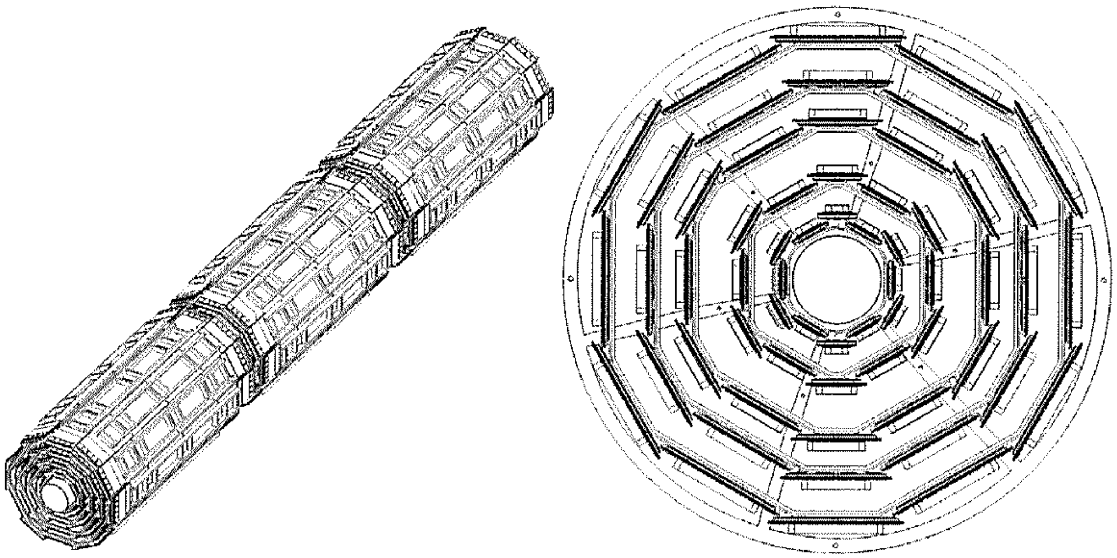

Figure 7: 3D view of the three barrels (left) and $r - \phi$ view of the barrel showing the 12 wedges with the 5 layers.

2.4.3 Intermediate Silicon Layers

Intermediate Silicon Layers (ISL) provides an extended forward coverage and links tracks between the COT and The SVX-II, and also can provide stand-alone 3D track information in the forward region. The ISL detector has one central layer at radius of 22cm covering

$|\eta| < 1.0$, and two forward layers at radii of 22cm and 28cm covering $1 < |\eta| < 2$, with total length of 3m. It is made of double-sided silicon with strips at a stereo angle of 1.2°, and a strip of 112μm. The breakdown voltage of the sensors is 100V limited by the breakdown voltage of the coupling capacitors.

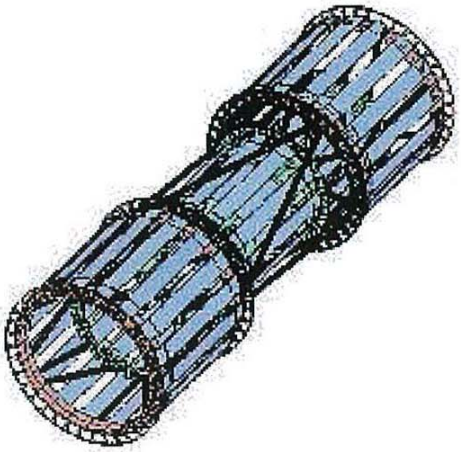

Figure 8: 3D veiw of the ISL spaceframe.

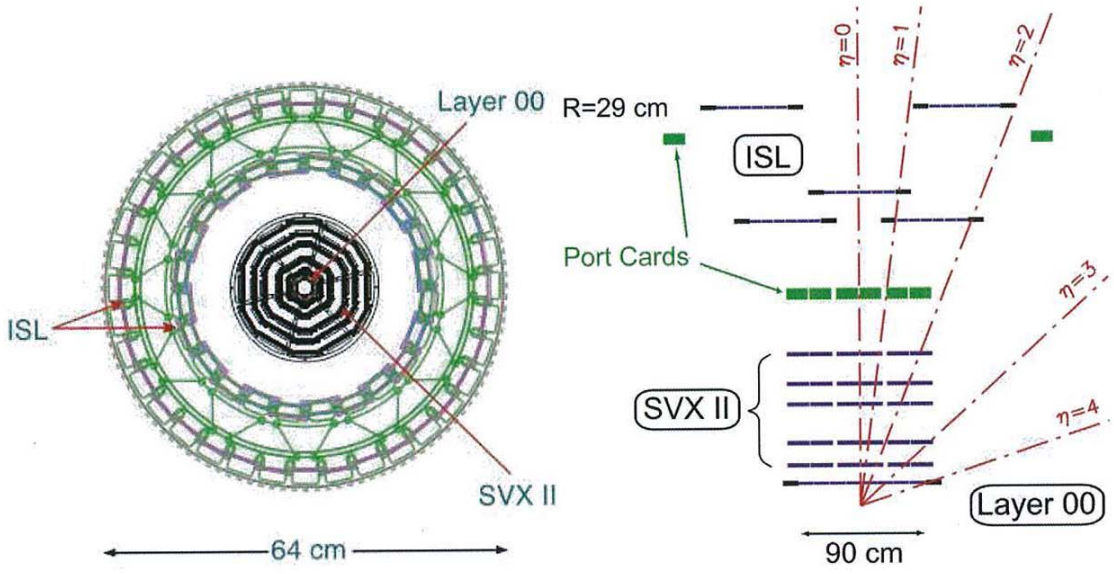

Figure 9: $r - \phi$ veiw (left) and $r - z$ view (right) of the silicon detectors.

2.4.4 Central Outer Tracker

The Central Outer Tracker (COT) is a cylindrical open-cell drift chamber spanning from 44 to 132cm in radii, and 310cm long. It operates inside a 1.4 Tesla solenoidal magnetic

field and is designed to find charged tracks in the region $|\eta| \leq 1.0$. The hit position resolution is approximately 140μm and the momentum resolution $\sigma(p_T) = 0.0015$ (GeV/c)$^{-1}$. The COT is segmented into 8 super-layers alternating stereo and axial, with a stereo angle of $\pm 2°$. Each super-layer contains 12 sense wires alternated with 13 potential wires which provide the field shaping within the cell yielding a total of 96 measurement layers. For the entire cell chamber, there are 30,240 sense wires and 32,760 potential wires. Operating with an Argon-Ethane (50:50) gas mixture the maximum drift time is approximately 180 ns. The cells ate tilted at 35° to account for the Lorentz angle such that the drift direction is azimuthal. Tracks originating from the interaction point which have $|\eta| < 1$ pass through all 8 superlayers of the COT. Tracks which have $|\eta| < 1.3$ pass through 4 or more superlayers. Table 3 shows a mechanical summary of the COT. Figure 10 shows cell layout for super-layer 2 (SL2). Figure 11 shows the east endplate slots sense and field planes.

Parameter	
Gas (Argon:Ethane)	(50:50)
Number of Layers	96
Number of Super-layers	8
Stereo Angle (degree)	+2, 0, −2, 0, +2, 0, −2, 0
Cells/Layers	168, 192, 240, 288, 336, 384, 432, 480
Sense Wires/Cell	12, 12, 12, 12, 12, 12, 12, 12
Radius at Center of SL (cm)	46, 58, 70, 82, 94, 106, 117, 129
Tilt Angle	35°
Material Thickness	1.6% X_0
Drift Field	1.9 kV/cm
Maximum Drift Distance	0.88 cm
Maximun Drift Time	177 ns
Number of Channels	30,240

Table 3: Design parameters of the Central Outer Tracker.

Figure 10: East endplate slots sense and field planes are at the clock-wise edge of each slot.

Figure 11: Nominal cell layout for SL2.

2.5 Calorimeter Systems

Segmented electromagnetic and hadron sampling calorimeters surround the tracking system and measure the energy flow of interacting particles in the $|\eta| < 3.6$. The calorimeter systems are divided into 2 systems with respect to the pseudo-rapidity range, central and plug(forward) region. The Central Electromagnetic Calorimeter (CEM) covers the $|\eta| < 1.1$, which uses lead sheets interspersed with polystyrene scintillator as the active medium and employs phototube readout. The Central Hadronic Calorimeter (CHA) covers the $|\eta| < 0.9$, which uses steel absorber interspersed with acrylic scintillator as the active medium. The plug calorimeters, Plug Electromagnetic Calorimeter (PEM) and Plug hadron calorimeter (PHA), cover the $1.1 < |\eta| < 3.6$. They are sampling scintillator calorimeters which are read out with plastic fibers and phototubes.

2.5.1 Central Calorimeter

The Central Electromagnetic Calorimeter detects electrons and photons and measures their energy. It is a lead-scintillator sampling system with tower segmentation, the each tower is 15° in $r - \phi$ plane. The CEM total thickness is 18 radiation length (32cm), to make sure that 99.7% of the electrons energy will be deposited. The CEM energy resolution is

$$\frac{\sigma_E}{E} = \frac{13.5\%}{\sqrt{E_T}} \oplus 2\% \tag{2.4}$$

where E_T is the transverse energy in GeV, $\oplus$ symbol means that the constant term is added in quadrature to the resolution, and position resolution is typically 2mm for 50 GeV/c electrons.

The Central Electromagnetic Showermax Chamber (CES) is used to identify electrons and photons using the position measurement to match with tracks, the transverse shower profile to separate photon from π^0s, and pulse hight to help identify electromagnetic showers. The CES is located at approximately 6 radiation lengths deep at the expected shower maximum of particles in the EM calorimeter. The CES module is a multi-wire proportional chamber with 64 anode wires parallel to the beam axis.

The Central Preshower Detector (CPR) is located at between the front face of the EM calorimeter and the magnet coil. The CPR can be useful in the $\pi-$photon separation and electron identification. The CPR was replaced the slow gas chamber with a faster scintillator version which has a better segmentation during RunII in 2004. The new CPR is used to improve the jet energy resolution.

The Central Hadronic Calorimeter is an iron-scintillator sampling calorimeter, covering range $|\eta| < 0.9$, approximately 4.5 λ_0 interaction length, and the energy resolution is

$$\frac{\sigma_E}{E} = \frac{50.0\%}{\sqrt{E_T}} \oplus 3\%. \tag{2.5}$$

The Wall Hadronic Calorimeter (WHA) also an iron-scintillator sampling calorimeter, covering range $0.7 < |\eta| < 1.3$. The WHA is 4.5 λ_0 interaction length, and the energy resolution is

$$\frac{\sigma_E}{E} = \frac{75.0\%}{\sqrt{E_T}} \oplus 4\%. \tag{2.6}$$

2.5.2 Plug Calorimeter

The plug calorimeter covers $1.1 < |\eta| < 3.6$, corresponding to polar angles $3° < \theta < 37°$ as shown in Figure 12. Each plug wedge spans 15° in azimuth, however from $1.1 < |\eta| < 2.11$ (37° to 14°) the segmentation in ϕ is doubled, and each tower spans only 7.5°. There is an electromagnetic section (PEM) with a shower position detector (PES), followed by a hadronic section (PHA).

The PEM is lead-scintillator sampling calorimeter, with unit layers composed of 4.5mm lead and 4mm scintillator. There are 23 layers in depth for a total thickness of about 21 X_0 radiation length at normal incidence. The PEM has an energy resolution is

$$\frac{\sigma_E}{E} = \frac{16\%}{\sqrt{E_T}} \oplus 1\%. \tag{2.7}$$

The PHA is an iron-scintillator sampling calorimeter, approximately 7 λ_0 in depth, and has an energy resolution of

$$\frac{\sigma_E}{E} = \frac{80\%}{\sqrt{E_T}} \oplus 5\%. \tag{2.8}$$

The PEM shower maximum detector is located about 6 λ_0 deep within the PEM, and is constructed of two layers of scintillating strips. The strips are 5mm wide, and roughly square in cross section. Position resolution of the PES is about 1mm. The summaries of design parameters for the calorimeter are shown in Table 4.

Calorimeter	Coverage	Energy Resolution (%)	Thickness	Absorber
CEM	$\|\eta\| < 1.1$	$13.5/\sqrt{E_T} \oplus 2$	18 X_0	3.18 mm lead
PEM	$1.1 < \|\eta\| < 3.6$	$16.0/\sqrt{E_T} \oplus 1$	21 X_0	4.5 mm lead
CHA	$\|\eta\| < 0.9$	$50.0/\sqrt{E_T} \oplus 3$	4.5 λ	2.5 cm iron
WHA	$0.7 < \|\eta\| < 1.3$	$75.0/\sqrt{E_T} \oplus 4$	4.5 λ	5.0 cm iron
PHA	$1.3 < \|\eta\| < 3.6$	$80.0/\sqrt{E_T} \oplus 5$	7.0 λ	5.08 cm iron

Table 4: Design parameters of the calorimeter.

2.6 Muon Detectors

Muons penetrate the tracking systems and the calorimeters leaving very little energy. The reason is muons produce much less bremsstrahlung than electrons and therefore do not produce electromagnetic showers, due to their larger mass. The CDF muon systems use this property by placing detectors behind enough material. Muons deposit minimum ionizing energy in the calorimeters matched with a track in the COT. The momentum of these muons is measured by their bend in the solenoidal field using the COT. The central muon system is capable of detecting with transverse momentum $p_T \geq 1.4$ GeV, through their interaction with the gas and subsequent drift on the produced electrons toward the anode wires. The muon detectors consist of four separate subsystems: the central muon

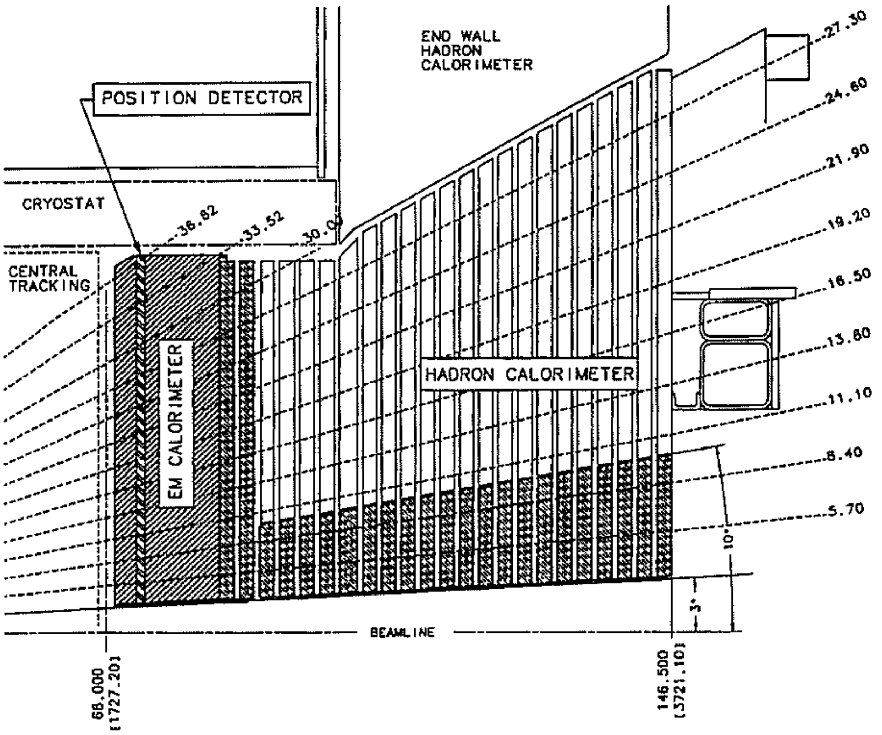

Figure 12: Cross section of the plug calorimeter (PEM and PHA).

chambers (CMU), the central upgrade (CMP), the central muon extension (CMX), and the barrel muon detector (BMU). Table 5 shows design parameters of the muon detector. Figure 13 shows the effective muon detector coverage in $\eta - \phi$ plane.

The CMU detector locates directly outside of the central hadron calorimeter, 35 m from the interaction point, and covers the region of $|\eta| \leq 0.6$. It is divided into 24 east and 24 west 15° wedges. Each wedge contains three muon chambers and each muon chamber consists of four layers of four rectangular drift cells staggered in order to eliminate hit position ambiguities. A stainless steel sense wire a diameter of 50μm is located in the center of each cell. A muon object is created by forming a "stub" from hits in the muon chambers matching it to an extrapolated COT tracks.

The CMP consists of a second set of muon chambers behind additional 60cm of steel in the region $55° \leq \phi \leq 90°$. The chambers are fixed length in z and form box around the central detector. The pseudorapidity coverage thus varies with azimuth as shown in Figure 13.

The central extension consist of conical section of drift tubes (CMX) in polar angle from 42° to 55° ($0.6 \leq |\eta| \leq 1.0$). The top two wedges (Wedge 5 and 6) of the west CMX is called the "Keystone". There are no top 2 wedge on the east CMX due to cryogenic utilities servicing the solenoid. The bottom 6 wedges (Wedge 15-20) are called "Miniskirt". The design parameters of the muon detector are shown in Table 5.

Muon detector	CMU	CMP	CMX
Coverage	$\|\eta\| < 0.6$	$\|\eta\| < 0.6$	$0.6 < \|\eta\| < 1.0$
Drift tube length [cm]	226	640	180
Max drift time [μs]	0.8	1.4	1.4
Total drift tubes	2304	1076	2208
Pion interation length (λ)	5.5	7.8	6.2
Minimum detectable muon p_T (GeV/c)	1.4	2.2	1.4

Table 5: Design parameters of the moun detector.

2.6.1 Luminosity Monitor

The beam luminosity has been measured using the process of inelastic $p\bar{p}$ scattering. The cross section is $\sigma_{\text{in}} \sim 60$ mb. The rate of inelastic $p\bar{p}$ interaction is given by

$$\mu f_{\text{BC}} = \sigma_{\text{in}} L \tag{2.9}$$

where L is the instantaneous luminosity, f_{BC} is the rate of bunch crossing in the Tevatron and μ is the average number of $p\bar{p}$ interaction per bunch crossing. In CDF Run II, Cherenkov luminosity counters (CLC) is used to measure the luminosity by counting number of $p\bar{p}$ interaction μ accurately.

The detector consists of two modules which are located in the "3 degree holes" inside the end-plug calorimeter in the forward and backward region and which cover $3.7 < |\eta| < 4.7$ range. Each CLC detector module consists of 48 thin, long, conical, gas-filled Cherenkov counters. The counters arranged around the beam pipe in three concentric layers, with 16 counters each, and pointing to the center of the interaction region. They are built with reflective aluminized mylar sheets of 0.1mm thick and have a conical shape. The cones in two outer layers are about 180cm long and the inner layer counters have the length of 110cm. The Cherenkov light is detected with fast, 2.5cm diameter, photomultiplier tubes. The tubes have a concave-convex, 1mm thick, quartz window for efficient collection of the ultra-violet part of Cherenkov spectra and operate at a gain of 2×10^5. The counters are mounted inside a thin pressure vessel made of aluminum and filled with isobutane. The systematic uncertainty of the luminosity measurement is dominantly coming from the uncertainty of the inelastic $p\bar{p}$ cross section ($\sim 3\%$), the CLC acceptance ($\sim 2\%$), and the non-lineality of the CLC acceptance due to CLC occupancy saturates as growing luminosity due to the finite number of counters ($< 2\%$).

2.6.2 Trigger Systems

The trigger plays an important role on hadron collider experiment because the collision rate is much higher than the rate as which data can be stored on tape. The crossing rate of the Tevatron under 36 on 36 bunch operation is 7.6MHz, corresponding to 396 ns collision separation. The role of the trigger is to effectively extract the most interesting physics events from the large number of minimum bias events. For Run II, CDF employs a three-level trigger system to selectively capture interesting events. The levels are denoted

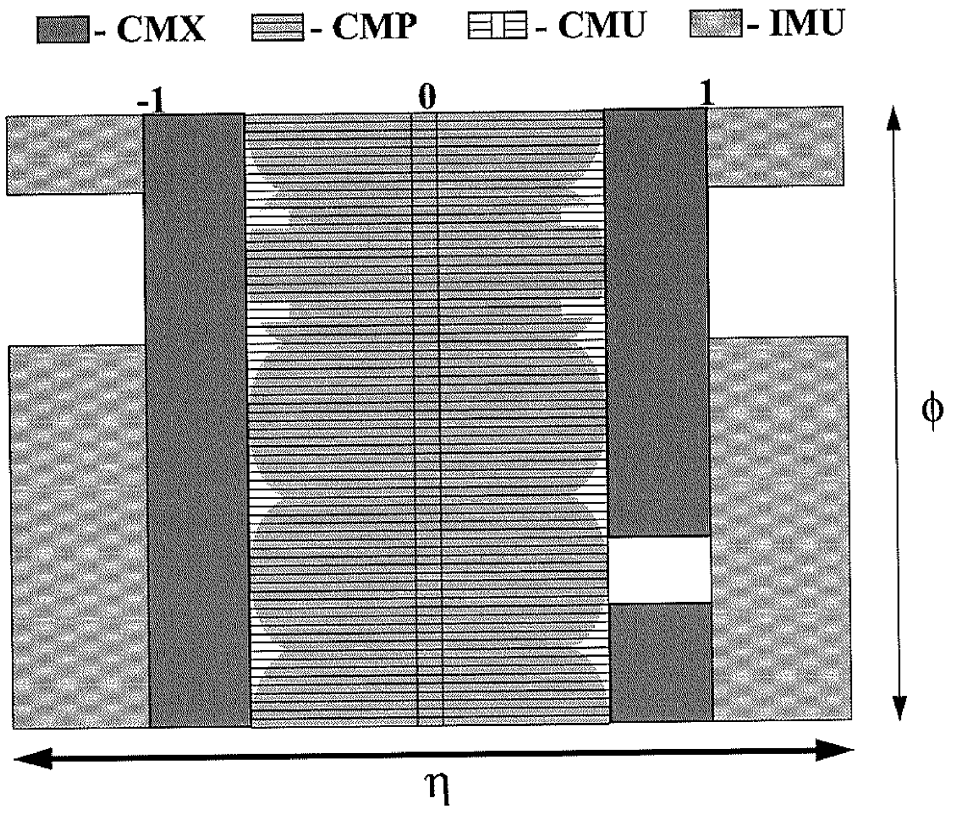

Figure 13: Muon detector coverage in $\eta - \phi$ plane.

simply as "L1", "L2" and "L3", with each subsequent level making more complicated decisions and requiring successively longer processing times. Figure 15 shows schematic of the CDF trigger system.

2.6.3 Level-1

The first level of trigger selection Level-1 (L1) uses custom designed hardware to find physics objects based on a subset of the detector information and then makes a decision based on simple counting of these objects. The input to the L1 hardware comes from the calorimeters, tracking chambers and muon detectors. The decision to retain an event for further processing is based on the number and energies of the electron, jet and muon candidates as well as the missing energy in the event, or on the kinematic properties of few of these objects. The L1 hardware consists of three parallel synchronous processing streams which feed inputs of the single Global Level-1 decision unit. One stream finds calorimeter objects, another finds muons and the third finds tracks in the central region. The L1 trigger can be formed using these streams singularly as well as AND or OR combinations of them. All elements of the L1 trigger are synchronized to the same 132ns clock, with a decision made every 132ns by Global L1. In the period of the data taking considered in this analysis the accelerator was the two intermediate clock cycles automatically rejected.

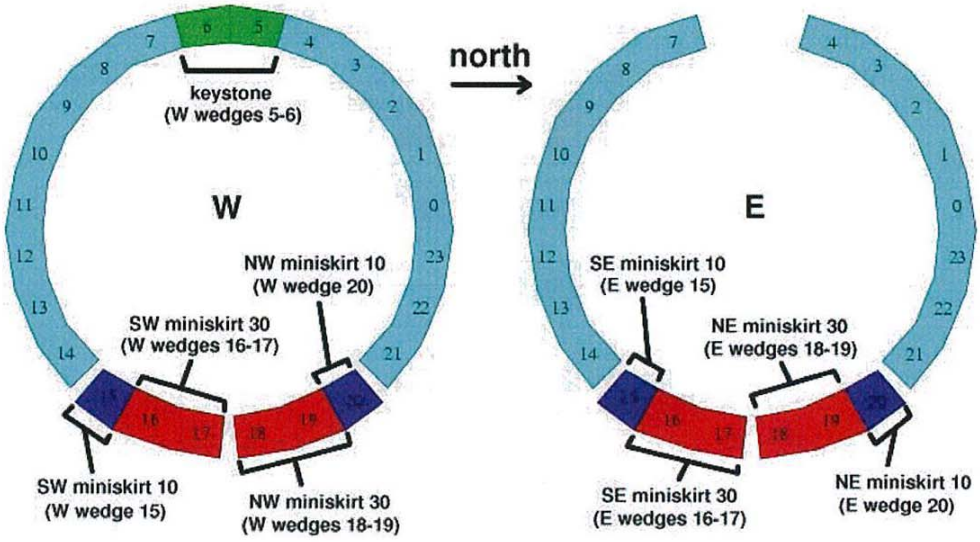

Figure 14: CMX detector in $r - \phi$ plane.

The maximum L1 accept rate is 20kHz, while the typical one is 12kHz.

2.6.4 Level-2

Events accepted by L1 are processed by the second level of trigger Level-2 (L2), which is composed of several asynchronous subsystems. These provide input data to programmable L2 processors on the Global L2 crate, which determine if any of the L2 trigger are satisfied. Processing for L2 trigger decision starts after the event written into one of the four L2 buffers by a L1 accept. When L2 is analyzing the event in one of the buffers, that buffer cannot be used additional L1 accept. If all the four are full, the deadtime of the data acquisition is increased. It follows that the time required for a L2 decision needs to be less than about 80% of the average time between L1 accepts in order to keep the deadtime as low as possible. For this purpose L2 has been pipelined into two stages each taking approximately 10μs, which is sufficient to keep the deadtime at a minimum, even if L1 had an accept-rate of 50kHz. The L2 buffers perform a limited event reconstruction using essentially all the information used in L1, but with higher precision. In addition, at L2, data from the central shower-max detector and the SVX are available, which improve respectively the identification of electrons and photons and the reconstruction of the secondary vertices. Furthermore, a jet reconstruction algorithm is provided by the L2 cluster finder. After all of the data are stored in the processors, the event is examined to check if the criteria of any of the L2 triggers have been satisfied. This operation can be performed while the new events are being loaded into memory, thus not affecting the dead time. The typical L2 accept rate, as of this writing, is between 100 and 300Hz, depending on the initial luminosity.

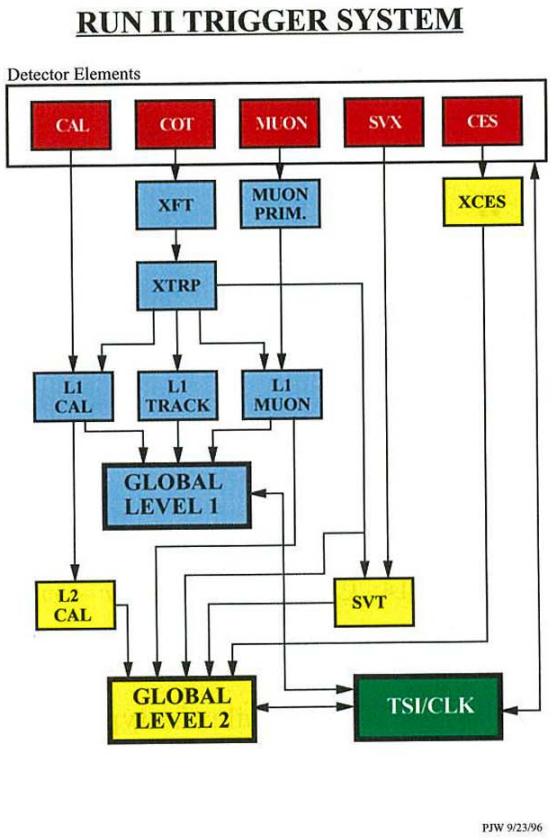

Figure 15: Book diagram of the trigger pass for Level 1 and Level 2.

2.6.5 Level-3

The Level-3 (L3) trigger subsystem is composed of two main components, the Event Builder (EVB) and the Level-3 Farm. Level-1 and Level-2 systems need to make their decisions at very high rate which makes it impossible to fully reconstruct each event. While Level-1 and Level-2 algorithms use small predefined pieces of event data to make their decision, the event pieces are stored in the buffers of the 140 Front End crates which constitute the EVB. After a L2 decision is made, the Event Builder assembles all event fragments from the Front End crates into one data block.

The 16 subfarms which compose the L3 Farm receive event fragments from the EVB and build complete events into the appropriate data structure for analysis. Since it takes about one second for one computer unit to make a trigger decision on one event, it takes a large farm of 250 Dual Pentiun Linux personal 5computers (called "processors") to ensure the required input rate. Each subfarm contains between 14 and 18 processor nodes and one "converter" node, which acts as "farm input" distributing the data flow coming from the EVB.

The events are then passed to a trigger algorithm (a different one for each processor) that categorizes the event and makes the decision as to whether or not to permanently store it. The selected event are passed to the Data Logger subsystem. During the

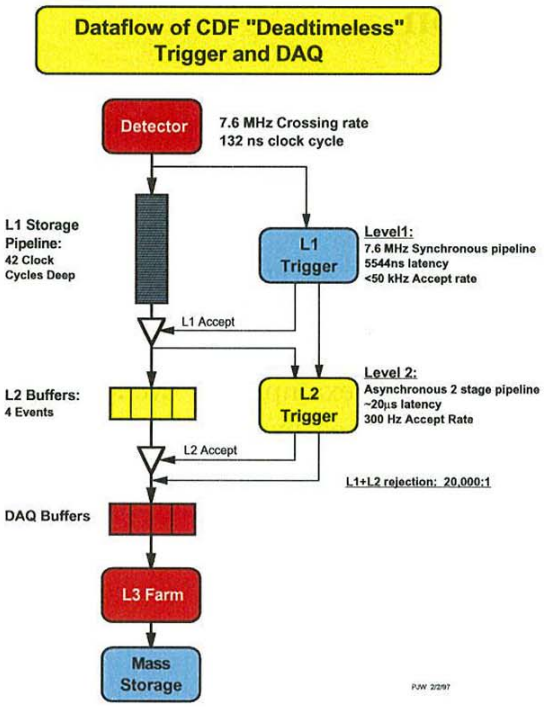

Figure 16: Schamatic diagram of the trigger and DAQ.

building processing, the event integrity is checked. The L3 algorithms take advantage of the full detector information and improved resolution unavailable to lower trigger levels. This includes full three-dimensional track reconstruction and tight matching of tracks to calorimeter and muon-system information. Results from the lower level are used or drive the algorithms, which are based on the off-line analysis packages. This is a modular and separated filter modules for specific triggers. L3 accept events with a rate of approximately 75Hz.

3 Event Selection

Physics objective in this thesis is to search for the diboson using high-p_T like-sign dilepton events (ee, $e\mu$, and $\mu\mu$), such event occurs in the following process,

$$q\bar{q}' \rightarrow W^{\pm}Z^0 \rightarrow \ell^{\pm}\ell^{\pm} + X. \tag{3.1}$$

The desirable events are collected by using trigger systems as described in previous chapter and series of lepton selection criteria in efficiently.

First, the trigger system collects the events roughly, however removes the undesirable events, i.e. background events, for example the event coming from inelastic $p\bar{p}$ collisions.

In second step, the event collected by trigger system are imposed the series of lepton selection criteria to reject the backgrounds as possible. The selection criteria are constructed by taken the lepton properties and the detector response for the leptons into account.

3.1 Dataset and Triggers

To collect the events efficiently, the data collected by inclusive high-p_T lepton (electron and muon) trigger is used.

The inclusive high-p_T electron trigger requires at least a electron satisfied the series of electron selection and some large E_T requirement. Some concretely speaking, the trigger selects the events have a object which deposit its some large energy to electromagnetic calorimeter ($E_T > 18$ GeV) and the energy deposition ratio (HAD/EM) is less than 0.124 and the lateral shower profile ($L_{\rm shr}$), and the position matching on z direction between CES and extrapolated track ($\Delta z_{\rm CES} < 8$cm). The criteria is applied to events in step by step, i.e. Level 1, Level 2, and Level 3, to reduce the data taking rate due to the capability limit for the trigger system. The trigger path are named `ELECTRON_CENTRAL_18_v*`, the asterisk symbol means the version number because of the trigger criteria are changed in run by run due to the performance and condition of CDF detector and Tevatron accelerator.

The inclusive high-p_T muon trigger requires at least a muon satisfied the series of muon selection and some large p_T requirement. The muon trigger are mainly categorized into CMUP moun trigger and CMX muon trigger, CMUP muon means a track object points to both CMU and CMP detector, while CMX muon points to CMX detector. The CMUP muon trigger is named `MUON_CMUP18_*`, which requires CMUP muon with XFT track $p_T > 18$ GeV/c and the position matching in x direction between the position on muon detectors, both CMU and CMP, and track. And the CMX muon trigger (named `MUON_CMX18_*`) requires CMX muon with $p_T > 18$ GeV/c and the position matching same as CMUP muon trigger however CMX detector.

The collected data are achieved during from 4th Feb. in 2002 to 16th Apr. in 2008 corresponding to an integrated luminosity 2.7 fb^{-1} data after run filtering for good detector condition and desirable, so-called "good run filtering". In CDF Run-II, the data is categorized to some dataset with respect to data taking span, ex. `0d`, or Period 0, to calibrate the data take into account the varying taking data condition due to long range operation.

3.2 Event Selection

As described before, the desirable events are high-p_T LS dilepton events to search for the diboson. CDF-II has well-defined algorithm to identify electrons or muons by using track reconstruction, energy clustering, and other particle proper reaction to detectors. The particle identifications are not used to effectively picking up desirable events, but reduce the background such as fake lepton. To further pick up the good events, there are more event selection criteria, as mentioned after sections.

3.3 Pre-Event Selection

The Pre-Event Selections are first used in several studies and estimations described in this thesis, for instance background estimations. One of them is used to ensure well-defined measurement of collisions with the detector. The selection requires the vertex with the highest p_T-sum of associated tracks, so-called "primary vertex", within the region in z plane, i.e. $|z_{\rm pv}| < 60$cm.

The Cosmic ray veto is also required as the Pre-Event Selection. The cosmic rays contaminate the physics event, coming from collision, by mimicking muons or electrons. While the cosmic rays are coming from outside of the detector, the muon with collisions are coming from center of detector. And the Cosmic rays cross the detector at any time with respect to the beam crossing. The cosmic ray veto is achieved to look at the direction of the trajectory and crossing timing.

3.3.1 Lepton Identification

The Electron Identification is achieved by using series of selection criteria, tracking and energy clustering, validated using test beam. Central electron (CEM), Central muon (CMUP and CMX) are only desirable object in the thesis, i.e. $|\eta|$ <1.2. The selections are categorized into 3 parts, "geometrical and kinematics cuts", "track quality cuts", and "identification cuts (ID cuts)".

3.3.2 Geometrical and kinematical cuts

- Electron Fiducial:
  This variable ensures that the electron is reconstructed in a region of the detector which well instrumented. The electron position in the CEM is determined using either the value determined by the CES shower or by the extrapolated track, and it must satisfy the following requirements.
  - The electron must lie within 21cm of the tower center in the $r-\phi$ view in order for the shower to be fully contained in the active region $|z_{\rm CES}| < 21$cm.
  - The electron should not be in the regions $|z_{\rm CES}| < 9$cm, where the two halves of the central calorimeter meet, and $|z_{\rm CES}| > 230$cm, which corresponds to outer half of the last CEM tower. This region is prone to leakage into the hadronic part of the calorimeter.

- The electron should not be in the region immediately closest to the point penetration of the cryogenic connections to the solenoidal magnet, which is uninstrumented. This corresponds to $0.77 < \eta < 1.0$, $75 < \phi < 90$ degree, and $|z_{\rm CES}| < 193$cm.

- Muon Fiducial:
  Muons are identified by matching hits in the muon chambers with a reconstructed track and energy in the calorimeter on the trajectory of the particle. The muons pass through the moun chambers, then the muon tracking is formed using the hit information and fitting algorithm (Muon (stub) reconstruction). The muon stub has at least three hits associated to it.

  - The fiducial distance of the tracks extrapolated to muon chambers in the $r-\phi$ plane and z-direction.
  - COT exit radius ρ:
    To ensure that CMX muon pass through all eight COT superlayers, CMX muons require COT exit radius ρ of the track. ρ is defined as,

$$\rho = \frac{\eta}{|\eta|} \cdot \frac{z_{\rm COT} - z_0}{\tan(\pi/2 - \theta)} \tag{3.2}$$

    where $z_{\rm COT}$ is used for the length of the COT (155cm).

- High transverse energy (E_T):
  The transverse electromagnetic energy deposited by electron is calculated as the electromagnetic cluster energy multiplied by $\sin\theta$, where θ is the polar angle provided by the best COT track pointing to the EM cluster.

- High transverse momentum (p_T):
  The transverse momentum of the COT track as measured by using the track curvature in the COT.

3.3.3 Track quality cuts

- COT hits requirement:
  To ensure that the track associated with the electron or muon is good quality reconstructed track, require that track has been reconstructed in the COT in 3 axial and 3 stereo superlayers with at least 7 hits in each.

- The relative position to primary vertex in z plane ($z_0 - z_{\rm pv}$):
  Separation between z coordinate of the closest approach point with respect to run average beam line (z_0) and primary vertex z position ($z_{\rm pv}$).

- Silicon hits requirement:
  The track is required hitting to some SVX layers (>3). The requirement critical plays to reject the residual photon conversion events which are considerable background in the LS dilepton events.

- Impact parameter (d_0):
  This variable is recalculated to take the x coordinate of the primary vertex. The cuts is the most powerfully for rejecting cosmic rays background.

3.3.4 Isolation cut

- Isolation ($\mathrm{ISO}^{\mathrm{cal}}_{0.4}$):
  The leptons are required to be isolated in terms of the calorimeter cone-isolation with cone size of $\Delta R = 0.4$ ($\Delta R = \sqrt{\Delta\eta^2 + \Delta\phi^2}$). The calorimeter isolation is defined for track objects. It is

$$\mathrm{ISO}^{\mathrm{cal}}_{0.4} = \sum_{\Delta R<0.4} E_T^{(i)} - (E_T^{(\mathrm{seed})} + E_T^{(\eta+1)} + E_T^{(\eta-1)}), \tag{3.3}$$

  where $E_T^{(i)}$ is the tower E_T summed over the electromagnetic and hadronic calorimeter, $E_T^{(\mathrm{seed})}$ is the E_T of the tower that the track is pointing, and $E_T^{(\eta\pm1)}$ is the same quantities for the towers in the same wedge but with the η index off by the 1 with respect to the seed tower.

3.3.5 Electron Identification cuts

- Ratio of hadronic and electromagnetic energy (HAD/EM):
  The ratio should be small, that is, energy deposition in electromagnetic calorimeter is much higher than energy deposition in hadronic calorimeter.

- EM shower shape (L_{shr}):
  The purpose of this quantity is to provide some discrimination of electrons and photons from hadronic showers faking these particles in the central electromagnetic calorimeter. This is done by comparing the observed the energy in CEM towers adjacent to the seed tower to expected electromagnetic shower taken with test beam data.

$$L_{\mathrm{shr}} = 0.14 \sum_i \frac{E_i^{(\mathrm{adj})} - E_i^{(\mathrm{exp})}}{\sqrt{(0.14\sqrt{E})^2 + (\Delta E_i^{\mathrm{exp}})^2}}, \tag{3.4}$$

  where E_i^{adj} is the measured energy in tower adjacent to the seed tower, E_i^{exp} is the expected energy in the adjacent tower from test beam data, $\Delta E_i^{\mathrm{exp}}$ is the error on the energy estimate.

- Ratio of the cluster energy to the momentum (E/p):
  If a object pointing calorimeter cluster is electron, its momentum measured by COT track matches to the energy in the calorimeter cluster, i.e. $E/p \sim 1$.

- The pulse height shape in CES (χ^2_{strip}):
  The pulse height shape in the CES detector in the $r - z$ view is compared to the test beam data using the χ^2 test.

- Track matching to CES cluster ($\Delta z_{\rm CES}$ and $Q \times \Delta x_{\rm CES}$):
  The extrapolated track is required to match a CES cluster in $r-\phi(x)$ and z plane. the $r-\phi$ plane requirement is asymmetry due to the trajectory of track in the detector. If the sign of charge and Δx is opposite, the track traverses a larger part of the calorimeter in adjacent towers, which results in more radiation and a less precise position.

- Conversion removal:
  A photon traveling through material converts into an electron-positron pair. However the electron is true electron, it not directly comes from hard scattering events (prompt electron). To remove the conversion electron, conversion tagging algorithm is used. The algorithm requires to opposite charge of electrons the following,

$$|\Delta\cot\theta| < 0.04, \text{ and } |\delta_{xy}| < 0.2, \tag{3.5}$$

  $\cot\theta$ is the difference between the polar angle cotangents of the tracks. δ_{xy} is the separation between the tracks in the $r-\phi$ plane.

3.3.6 Muon Identification cuts

- Small calorimeter deposition (EM and HAD):
  Muons deposit small energy in the calorimeters due to minimum ionization. The energy deposition in the calorimeter increases linearity with moun momentum, and consequently the cut efficiency loss. To maintain good efficiency for high momentum muon, the cut is taken into account for the momentum dependence.

- Track-stub matching in $r-\phi$ plane ($r \times \Delta\phi$):
  The track is required to match the muon stub in $r-\phi$ plane.

3.3.7 Jet Reconstruction

Quark and gluon particles are observed as "jet" objects due to its fragmentation and radiation effects, as a results construct shower of particles. The energy of jet are calculated from the energy deposited in the calorimeter towers using a cone clustering algorithm with a fixed cone size in which the center of the jet is defined as (η^{jet}, ϕ^{jet}) and the size of the jet cone as $R = \sqrt{(\eta^{tower} - \eta^{jet})^2 + (\phi^{tower} - \phi^{jet})^2} = 0.4$. The jet clustering algorithm groups calorimeter towers with $E_{Ti} < 1$ GeV. The algorithm is performed by first defining "Seed towers" has largest E_{Ti}. The seed tower are used to build "clusters" with size $R = 0.4$. The cluster transverse energy and its position is calculated as the follows,

$$E_T^{jet} = \sum_{i=0}^{N} E_{Ti}, \ \phi^{jet} = \sum_{i=0}^{N} \frac{E_{Ti}\phi_i}{E_T^{jet}}, \ \eta^{jet} = \sum_{i=0}^{N} \frac{E_{Ti}\eta_i}{E_T^{jet}} \tag{3.6}$$

where N is the number of towers inside the radius R with $E_{Ti} > 1$ GeV. This procedure is repeated until the cluster centroid is stable. Overlapping jets are merged if they overlap by more than 50%. If the overlap is smaller than 50%, each tower in the overlap region is assigned to the nearest jet. The measured jets are corrected to particle jet level or

parent parton level by taking into account for the detector effects and for radiation and fragmentation effects. The collected jet transverse momentum is expressed as the follows,

$$\begin{aligned} p_T^{parton} &= (p_T^{jet} \times C_\eta - C_{\rm MI}) \times C_{\rm Abs} - C_{\rm UE} + C_{\rm OOC} \\ &= p_T^{particle} - C_{\rm UE} + C_{\rm OOC}, \end{aligned} \tag{3.7}$$

where p_T^{parton} is the transverse momentum of the parent parton, which is taken into account for all effects, p_T^{jet} is the transverse momentum measured in the calorimeter, $p_T^{particle}$ is the transverse momentum of the particle jet, which is corrected for detector effects, and

- C_η is "η-dependent" correction. The correction takes into account variations in calorimeter response and gain as a function of jet η
- $C_{\rm MI}$ is "Multiple Interaction" correction, which is the energy coming from multiple $p\bar{p}$ interaction in the same bunch crossing to subtract from the jet
- $C_{\rm Abs}$ is "Absolute correction", is the correction of the calorimeter response to the momentum of the particle jet
- $C_{\rm UE}$ is "Underlying Event correction", to remove energy coming from underlying event such as initial state radiation and beam-beam remnant
- $C_{\rm OOC}$ is "Out-of-Cone correction" is correction of parton radiation and hadronization effects due to the finite size of the jet cone algorithm

The collections are performed by using the generic jet samples and MC samples generated by several generators (PYTHIA and HERWIG), and The systematic uncertainties coming from these collections also estimated. The systematic contribution mainly arise from the absolute jet energy collection due to difference between data and MC for calorimeter response (2%). The total systematic uncertanity is decreasing $\sim$ 8% to $\sim$ 2% as the jet energy increases (0 to >80 GeV).

3.3.8 Missing Transverse Energy

However neutrinos cannot be detected with CDF detector, its energy will manifest as missing energy. The CDF uses "missing transverse energy ($\not\!\!E_T$)" taking into account for transverse energy imbalance because of the missing energy, the vector sum of transverse energies should be ideal null. The missing transverse energy is measured using the transverse energy imbalance,

$$\not\!\!E_T = -\sum_i E_T^{(i)}, \tag{3.8}$$

where $E_T^{(i)}$ is the transverse energy of ith calorimeter tower. It need to be corrected for the muon minimum ionization energy taking into account for muon momentum measured by tracking.

3.4 Like-Sign Dilepton Event Selection

The final desirable events in this thesis are like-sign dilepton events to search for the diboson. To collect the events, the series of selection as mentioned in § 3.2 are applied to the data corresponding to an integrated luminosity of 2.7 fb^{-1}. In the selection, the applied transverse energy or momentum requirement to dilepton is asymmetric. If the 1st lepton is

- electron, $E_T > 20$ GeV and $p_T > 10$ GeV/c
- muon, $p_T > 20$ GeV/c

while, if the 2nd lepton is

- electron, $E_T > 6$ GeV and $p_T > 6$ GeV/c
- muon, $p_T > 6$ GeV/c

where the 1st lepton type is required to match trigger path, that is, when the 1st lepton is electron, the trigger path should be `ELECTRON_CENTRAL_18_v*`. The event selections are listed in Table 6.

Event pre-selection	
$\lvert z_{\rm pv}\rvert < 60$ cm	
Cosmic-ray veto	
Electron selection	**Muon selection**
Geometrical and kinematical cuts	
CEM	CMUP or CMX
Fiducial	Fiducial (CMUP), $\rho_{\rm COT} > 140$ cm (CMX)
	Blue-beam veto, keystone veto, miniskirt veto
$E_T^{\ell_1} > 20$ GeV ($p_T > 10$ GeV/c)	$p_T^{\ell_1} > 20$ GeV/c
$E_T^{\ell_2} > 6$ GeV ($p_T > 6$ GeV/c)	$p_T^{\ell_2} > 6$ GeV/c
Track quality cuts	
Axial ≥ 3 and stereo ≥ 3 (≥ 7 hits)	
$\lvert z_0 - z_{\rm pv}\rvert < 2$ cm	
Silicon hits ≥ 3	
$\lvert d_0\rvert < 0.02$ cm	
Isolation cut	
$\mathrm{ISO}_{0.4}^{\rm cal} < 2$ GeV	
Identification cuts	
HAD/EM $< 0.055 + 0.00045 \times E$	EM $< \max(2, 2 + 0.0115 \times (p - 100))$ GeV
$L_{\rm shr} < 0.2$ ($E_T < 70$ GeV)	HAD $< \max(6, 6 + 0.0280 \times (p - 100))$ GeV
$E/p < 2$ ($E_T < 50$ GeV)	$\lvert r \times \Delta\phi\rvert < 3, 5, 6$ cm (CMU, P, X)
$\chi^2_{\rm strip} < 10$	
$\lvert\Delta z_{\rm CES}\rvert < 3$ cm	
$-3.0 < Q \times \Delta x_{\rm CES} < 1.5$ cm	
Other cuts	
Conversion removal	

Table 6: Event pre-selection and lepton selection cuts.

Exactly two leptons
$\lvert z_0^{\ell_1} - z_0^{\ell_2}\rvert < 2$ cm
Dilepton mass > 12 GeV/c^2
At least one like-sign pair

Table 7: Dilepton selection cuts.

Track object
Opposite-sign
$p_T > 10$ GeV/c
track cone-isolation < 4 GeV/c
axial ≥ 3 and stereo ≥ 2 (≥ 5 hits)
$\lvert z_0 - z_{\rm pv}\rvert < 10$ cm
EM object
$E_T > 10$ GeV
HAD/EM < 0.12
fractional isolation $\mathrm{ISO}^{\rm cal}_{0.4}/E_T < 0.15$
Muon object
$p_T > 10$ GeV/c
EM < 5 GeV
HAD < 10 GeV
fractional isolation $\mathrm{ISO}^{\rm cal}_{0.4}/p_T < 0.15$
$\lvert z_0 - z_{\rm pv}\rvert < 10$ cm
$\lvert d_0\rvert < 0.5$ cm

Table 8: Physics objects used to identify.

4 Acceptance and Efficiency

$$WZ \to (\ell^{\pm}\nu)(\ell^{+}\ell^{-}) \tag{4.1}$$

Check were made to confirm the modeling of the data by the Monte Carlo and the validity of the trigger efficiency and scale factors. It is important for the Monte Carlo to be normalized correctly, as too many or too few data events due to badly normalized Monte Carlo may be incorrectly interpreted as a real absence or abundance of signal events. Similarly, if the Monte Carlo is mis-modelled in the variable utilized by the analysis, an apparent excess or deficiency may be caused by a mismatch of data events lying in the wrong phase space region.
The MC samples were generated by PYTHIA generator. The MC data are all applied with the relevant scale factors that are discussed in the below. A rather important point regarding our MC prediction is that residual photon-conversions and fake-leptons including non-prompt leptons from (semi-)leptonic decays of heavy-flavor hadrons found in the MC events are explicitly removed from the MC contributions by looking at the `OBSP` information since their contributions are assumed to be directly estimated from the data-driven methods.

4.1 Monte Carlo Scale Factors

The scale factor (SF) is to be used in MC based events yield estimation. The event yield N is driven by

$$N = L \cdot \varepsilon \cdot \sigma, \tag{4.2}$$

where L is the integrated luminosity, ε is the total detection efficiency, and σ is the process cross section. The total detection efficiency includes several selection efficiency, can be expressed as,

$$\varepsilon = \sum_i A^{(i)} \cdot \varepsilon^{(i)}_{\text{trig}} \cdot \varepsilon^{(i)}_{\text{pre}} \cdot \varepsilon^{(i)}_{\text{ID}} \tag{4.3}$$

where i means dilepton types such as CEM-CEM, CMUP-CMX and so on. $A^{(i)}$ is geometrical and kinematical acceptance, $\varepsilon^{(i)}_{\text{trig}}$ is trigger efficiency, $\varepsilon^{(i)}_{\text{pre}}$ is pre-selection efficiency, and $\varepsilon^{(i)}_{\text{ID}}$ is lepton identification efficiency.

The trigger efficiency is driven by using real data, while other efficiencies are driven by data and MC samples, respectively. The MC based event yield are scaled by the ratio of the efficiency in data and MC to more match MC yield to real data. In this thesis, the estimated scale factor are pre-selection efficiency and lepton identification efficiency.

4.2 Data Samples

As described in §3.1, the data collected by inclusive high-p_T lepton trigger is used to search in the diboson. The employed triggers are `ELECTRON_CENTRAL_18`, `MUON_CMUP18`, and `MUON_CMX18`, the trigger efficiencies is used in the total detection efficiency.

The triggers can effectively collect the electroweak process events such as Drell-Yan events. The Drell-Yan events are used to estimate the lepton identification efficiency. The Drell-Yan MCs are used to estimate the efficiency in MC, which are generated by PYTHIA.

4.3 Trigger Efficiency

The trigger efficiencies are estimated period by period from the period 0 through 17 to take the changes of trigger tables into account as much as possible.

4.3.1 High-p_T Electron Trigger Efficiency

The electron trigger efficiency is estimated for the parts of the tracking trigger and the calorimeter trigger, separately. We use the W_NOTRAK trigger to estimate tracking trigger efficiency. The W_NOTRAK trigger has the same calorimeter trigger path as the ELECTRON_CENTRAL_18 trigger path, but does not have the tracking trigger path. For the tracking trigger efficiency, we pick up W candidate events which have good electrons passing our electron selections, missing $E_T > 25$ GeV, and W_NOTRAK trigger bits. These are the denominator of the efficiency. Then we require the tracking trigger at each level to estimate the efficiencies.

For the Level-1 calorimeter trigger efficiency, we use high-p_T muon samples as unbiased samples. In moun samples, we pick up good electrons passing our electron selections (the L1 denominator), then require the event to fire the L1_EM8 trigger (the L1 numerator). The L1_EM8 trigger is the same as the Level-1 trigger of ELECTRON_CENTRAL_18 (L1_CEM8_PT8) for calorimeter trigger part. For the Level-2 calorimeter trigger efficiency, we use good lepton events which are triggered by the ELECTRON_CENTRAL_18_NO_L2 and the Level-1 trigger of ELECTRON_CENTRAL_18 (the L2 denominator), then we require the Level-2 trigger of ELECTRON_CENTRAL_18 (the L2 numerator). For the Level-3 calorimeter trigger efficiency measurement, first we pick up good lepton events passing the ELECTRON_CENTRAL_18_NO_L2 and the Level-2 trigger of ELECTRON_CENTRAL_18 (the L3 denominator), moreover we require the Level-3 trigger (the L3 numerator).

4.3.2 High-p_T Muon Trigger Efficiency

We use $Z \rightarrow \mu\mu$ events which have the invariant mass between 81 to 101 GeV/c^2 and fire the MUON_CMX18 (MUON_CMUP18) trigger to estimate the MUON_CMUP18 (MUON_CMX18) trigger efficiency (the denominator events). Then we apply the MUON_CMUP18(MUON_CMX18) trigger. We just require dileptons in events, no jet objects, so this muon trigger efficiency is not including the Jet10 trigger.

4.4 Primary-vertex Cut Efficiency and Scale Factor

Primary-vertex cut is to select events within the detector region well-defined measurement of collisions. The region is confirmed as $|z_{\rm pv}| < 60$cm by using cosmic ray and simulation. The cosmic ray track z_0 and simulation z_0 finding efficiency both indicate that the finding efficiency within $|z_0| < 60$cm is flat. The acceptance with the $p\bar{p}$ beam luminous region of $|z_0| < 60$cm is determined by fitting to "Beam Luminosity Function" with $|z_0| < 60$cm. The beam luminosity function is the longitudinal profile of the luminous region, expressed by

$$\frac{dL(z)}{dz} = N_p N_{\bar{p}} \frac{1}{\sqrt{2\pi}\sigma_z} \frac{\exp(-z^2/2\sigma_z^2)}{4\pi\sigma_x(z)\sigma_y(z)} \tag{4.4}$$

where z is primary-vertex position, $N_{p,\bar{p}}$ are proton or antiproton beam fluxes, and $\sigma_{x,y,z}(z)$ are the beam widths. The efficiency is calculated from the fit to z of beam profile as follows,

$$\varepsilon(|z_0| < 60\text{cm}) = \frac{\int_{-60}^{+60} [dL(x)/dz]dz}{\int_{-\infty}^{+\infty} [dL(z)/dz]dz}. \tag{4.5}$$

We are using high-p_T lepton trigger samples, Drell-Yan Monte Carlo and WZ Monte Carlo samples.

4.5 Lepton Selection Efficiency and Scale Factor

We estimate lepton selection efficiency based on our like-sign dilepton analysis. Our base kinematical-cut is $p_T > 20$ GeV/c for the leading lepton and $p_T > 6$ GeV/c for the 2nd leading lepton, so we look at the efficiency and scale factor from $p_T > 6$ GeV/c. We use Drell-Yan events of the data and MC samples which are produced by PYTHIA to estimate the efficiency and scale factor. For the electron selection efficiency, we estimate it in 2 regions with respect to electron E_T, because the scale factor of electron identification cut depends on electron E_T. We decide to divide the efficiency and scale factor to 2 region at $E_T = 30$ GeV, while the scale factor does not show any clear dependence on the muon p_T. The estimated cut variables are shown in Table 6.

4.6 OSLS Fake Ratio

We use Drell-Yan events to estimate the efficiency and scale factor. The Drell-Yan events are opposite sign dilepton events which are passing $\Delta\phi_{\ell_1\ell_2} > 2.8$ (rad) cut. Such Drell-Yan events contain non-negligible amount fake backgrounds in the events, in particular when the 2nd leading lepton is low p_T. So, we subtract the backgrounds from the Drell-Yan events to get more pure Drell-Yan events using a ratio of opposite sign(OS) fake events and like sign(LS) fake events (R_{OSLS}). The Drell-Yan counting method is

$$N_{\text{DY}} = N_{\text{OS}} - N_{\text{LS}} \times R_{\text{OSLS}}, \tag{4.6}$$

$$R_{\text{OSLS}} = \frac{\text{The number of fake OS events}}{\text{The number of fake LS events}}, \tag{4.7}$$

where N_{OS} is the number of OS dilepton events, N_{LS} is the number of LS dilepton events. the dilepton events have the 1st leading lepton passing all lepton selection cut and the 2nd leading lepton passing geometrical, kinematical cut and any selection cut. we define the fake Drell-Yan event as the 1st leading object is passing all lepton selection criteria and the 2nd leading object is satisfied geometrical and kinematical cut and hadronic object criteria (HAD/EM > 0.2, HAD > 1.0 GeV and EM > 4 GeV). We regard such a diobject event as fake Drell-Yan event. If we simply regard the LS dilepton events as background, we go into underestimate the background, because real dilepton events have charge correlation as mentioned in §5.1.4. We require the reading lepton passing all the lepton selection and the event fire the high-p_T lepton trigger. Then we apply our lepton selections to the 2nd

lepton, as a probe, passing only the geometrical and kinematical selections. If the dilepton type contains the same type of lepton objects such as CEM-CEM, CMUP-CMUP, and CMX-CMX, the efficiency is calculated by

$$\varepsilon = \frac{2 \times N_{\text{after}}}{N_{\text{before}} + N_{\text{after}}}, \tag{4.8}$$

while if it consists of different types, the efficiency is given by

$$\varepsilon = \frac{N_{\text{after}}}{N_{\text{before}}}, \tag{4.9}$$

where the N_{before} is the number of events before a selection and the N_{after} is the number of events after a selection.

4.7 Low-E_T Electron Selection Efficiency and Scale Factor

We estimate the electron selection efficiency and scale factor for low-E_T electrons ($E_T < 30$ GeV) using Drell-Yan events ($\Delta\phi_{\ell_1\ell_2} > 2.8$), the events are provided by extracting LS dielectron events applied OSLS ratio from OS dielectron events with the invariant mass greater than 20 GeV/c^2. As mentioned before, the identification scale factor depends on the E_T of electron.

4.8 High-E_T Electron Selection Efficiency and Scale Factor

We estimate the electron selection efficiency and scale factor for high-E_T electrons ($E_T >$ 30 GeV) using Drell-Yan events within Z mass window ($76 < M_{ee} < 106$) and the background subtraction is same as low-E_T electron selection efficiency study (see §4.7).

4.9 Muon Selection Efficiency and Scale Factor

We estimate the muon selection efficiency and scale factor using Drell-Yan events with OSLS ratio to subtract background events. In muon case, there is no clear muon p_T dependence for any muon selection variables.

4.10 Muon Reconstruction Efficiency and Scale Factor

We use Drell-Yan event passing $\Delta\phi_{\ell_1\ell_2}$ cut (> 2.8), the difference of z_0 position criterion for dimuon ($|z_0^{\ell_1} - z_0^{\ell_2}| < 2$cm) to estimate the muon reconstruction efficiency. we also use OSLS ratio to subtract the background. We are using the high p_T muon trigger samples and Drell-Yan MC data produced by PYTHIA.

4.11 $Z/\gamma^* \to \ell^+\ell^-$ Cross Section

We measure the $Z/\gamma^* \to \ell^+\ell^-$ cross section for the invariant mass region 66-116 GeV/c^2 using the trigger efficiency and the scale factors to validate them. The cross section can be expressed by

$$\sigma(Z/\gamma^* \to \ell^+\ell^-) = \frac{N_{\text{obs}}}{L \cdot \varepsilon}, \tag{4.10}$$

$$\varepsilon = \varepsilon_{\mathrm{MC}} \cdot \varepsilon_{\mathrm{trig}} \cdot \mathrm{SF}_{\mathrm{pv}} \cdot \mathrm{SF}_{\ell_1} \cdot \mathrm{SF}_{\ell_2} \,, \tag{4.11}$$

the N_{obs} is the number of observed events, the L is the integrated luminosity, the $\varepsilon_{\mathrm{MC}}$ is $Z/\gamma^* \to \ell^+\ell^-$ efficiency derived by Drell-Yan MC samples. the $\varepsilon_{\mathrm{trig}}$ means lepton trigger efficiency, the $\mathrm{SF}_{\mathrm{pv}}$ is the scale factor for the primary-vertex cut efficiency, and the $\mathrm{SF}_{\ell_{1,2}}$ mean the lepton selection and muon reconstruction efficiency scale factors. We see the maximum 8.0% difference in observed event and expected event for CMX-CMUP pair. We consider the overall difference (2.8%) as systematic uncertainty for our like-sign dilepton analysis.

5 Background

Although the LS requirement is quite effective to suppress QCD and known electroweak processes, fake-lepton backgrounds including non-prompt leptons such as those from photon conversions or from heavy-flavor decays, as well as literal fake leptons, still remain at a considerable level in the events of our signature. They are estimated by using data and MC samples, and the contributions of residual photon-conversion which survived our conversion veto are separated from the rest of the fake-lepton backgrounds by knowing the conversion detection efficiency and the number of identified conversions. While other backgrounds which is containing prompt real lepton are estimated by using MC data.

5.1 Fake Leptons

Fake leptons are one of major backgrounds in the like-sign (LS) dilepton events. They were estimated by weighting lepton + isolated track events with the expected fake-lepton yield for a given isolated track. These rates used to estimate fake-lepton backgrounds are called the fake-lepton rates, and are defined with respect to some reference rates, the rates of denominator objects. It is expected that the simple isolated-tracks in the OS combination are significantly contaminated by real leptons from Drell-Yan processes, which leads to overestimates of fake-lepton backgrounds. To avoid this problem and to establish a consistent scheme which can be applied to both the OS and LS cases, we choose isolated tracks that deposits certain energies in the electromagnetic (EM) and hadron (HA) calorimeters in the way such that they are not likely to be induced by real leptons.

5.1.1 Fake-lepton Backgrounds

The lepton plus fake-lepton backgrounds arise typically from a single lepton event such as $W \rightarrow \ell\nu$. This type of backgrounds consist of one trigger lepton and one fake lepton. The components of the "fake lepton" are

- Fake leptons
  1. Interactive $\pi^{\pm} \rightarrow$ fake electrons,
  2. Overlap of π^0 and a track $\rightarrow$ fake electrons,
  3. Punch-through hadrons $\rightarrow$ fake muons,
- Non-prompt leptons
  1. Residual photon conversions $\rightarrow$ electrons
  2. Decay-in-flight muons from $\pi^{\pm}$ and $K^{\pm} \rightarrow$ muons,
  3. (Semi-)Leptonic decay of heavy-flavor hadrons $\rightarrow$ leptons.

As noted here, we use "fake leptons" as a generic word to mean both the literal fake leptons and non-prompt leptons. Most of the components are considered to be non-isolated and quite common in generic QCD events, while the residual photon-conversions are not

necessarily QCD specific, and they are separately estimated from identified conversions with a similar philosophy as the fake-lepton rates. Correspondingly, contributions of residual conversions are subtracted from fake-electron rates in this study.

5.1.2 Measurement of Fake-lepton Rates

We define the fake rate R_{fake} as a rate of fake leptons relative to isolated tracks with certain energy depositions especially in the hadron calorimeters, which we call "hadronic" tracks:

$$R_{\text{fake}} = \frac{\text{lepton objects passing nominal selections and considered to be fakes}}{\text{isolated tracks with required calorimeter energy depositions}}. \quad (5.1)$$

It is noted that we define the fake rate here per isolated track, not per jet. The event pre-selection and the isolated hadronic-track selection criteria are listed in Table 9. The kinematical cut is $p_T > 6$ GeV/c and we require the same track-quality cuts as shown in Table 6. The hadronic-track selection imposes cuts on the energy depositions in the calorimeter towers that a given track is pointing. The first cut in the table is thought to mainly reject real electrons and the other cuts are meant to reject real muons. As to the numerator, we apply the nominal lepton selection cuts to find fake-lepton objects.

We evaluate R_{fake} using inclusive jet samples. The data we use are the `Jet20`, `Jet50`, `Jet70`, and `Jet100` generic jet samples from the `0d` through the `0i` datasets. The "jet samples" means different types of jet data collected by different triggers. In order to remove real-leptons from the numerator side, we impose a W veto and a Z veto. The W veto rejects events with

- electrons with $E_T > 20$ GeV or muons with $p_T > 20$ GeV/c passing lepton selection shown in Table 6,
- $\not\!\!E_T > 30$ GeV or transverse mass > 40 GeV/c^2.

The $\not\!\!E_T$ is corrected for muons passing our muon selection with the $p_T > 6$ GeV/c cut. The Z veto rejects events with

- electrons with $E_T > 20$ GeV or muons with $p_T > 20$ GeV/c passing our lepton selection,
- invariant mass with the 2nd-leg objects is in the mass window of 81–101 GeV/c.

The definition of the 2nd-leg objects for the Z veto is given in Table 8. Note that the EM objects for the 2nd-leg are not necessarily in the central region. Finally, we require the hadronic tracks and fake-lepton objects be both separated from the trigger jet in the η-ϕ space by $R > 1.0$ to remove possible trigger biases.

5.1.3 Subtraction of Residual Photon-Conversions

Residual photon-conversions in the fake-electron objects found in the jet samples are estimated from the amount of identified conversions multiplied with weights for residual photon-conversions inferred from them, which we refer to as residual conversion ratios. In this case, the uncertainties shown in the figure include a systematic uncertainty from the residual conversion estimation, quantified by $\pm 1\sigma$ variations of the residual conversion ratios, as well as the RMS spread over the jet samples.

Event pre-selection
$\lvert z_{\rm pv}\rvert < 60$ cm
Cosmic-ray veto
Geometrical and kinematical cuts
CDF default tracks in the central region
$p_T > 6$ GeV/c
Track quality cuts
axial ≥ 3 and stereo ≥ 3 (≥ 7 hits)
$\lvert z_0 - z_{\rm pv}\rvert < 2$ cm
Silicon hits ≥ 3
$\lvert d_0\rvert < 0.02$ cm
Isolation cut
$\mathrm{ISO}^{\rm cal}_{0.4} < 2$ GeV
Hadronic-track selection
HA/EM > 0.2
EM > 1 GeV
HA > 4 GeV

Table 9: Event pre-selection and the denominator track selection.

5.1.4 Real-lepton Contamination and Charge Correlation

In this section, we briefly check an implication of hadronic-track selection in applications to inclusive lepton data. For this plot, the track object search in a given event is performed only when there is exactly one good muon passing all the muon selection cut with the high p_T cut of $p_T > 20$ GeV/c. Also, the simple isolated tracks in this analysis are checked if they are associated with any good leptons or any EM objects with conversion flags, and removed if so. The $\mu\mu$ events and the μ + isolated-track events are therefore mutually exclusive.

First of all, we can confirm from a strong Z peak that simple isolated tracks of the OS case are significantly contaminated by real muons. Since the fake-muon rates are about at a few % level as obtained in the previous sections, the estimated fake backgrounds from the isolated tracks would be also a few % level of dimuon candidates. It is actually not a serious problem compared to the large contributions from real dimuon events, although the estimated value of fake backgrounds itself would be orders of magnitude larger than the correct answer. We also see that the isolated track rates get larger than those of the dimuon candidates toward low mass regions, which indicate more backgrounds at low masses as expected. For the case of isolated hadronic tracks, the situation is greatly

improved. We are picking up relatively more backgrounds with suppressing real muon contamination. Remembering again the fake-muon rates are about a few %, the fake-lepton backgrounds are negligibly small in the OS dimuon events in rather a wide invariant mass range.

One of interesting thing is a comparison between the OS and LS combinations of μ + hadronic tracks. The OS rates are larger than the LS rates even outside Z mass regions, which could be a sign of charge correlation besides the effects due to real dimuon events. In order to get a better measure, we investigate real-muon contamination in the hadronic tracks with helps of PYTHIA Monte Carlo (MC) events. We use inclusive $W \to \mu\nu$, $Z \to \mu\mu$, and $Z \to \tau\tau$ MC samples to collect μ + hadronic tracks, and compare with the data. We see that the observed μ + hadronic tracks are qualitatively described by MC events, and also see that contributing mass regions are different between the processes. The gradual rise of the rates toward low mass regions can be understood as coming mainly from contributions of W events. The MC predictions of the absolute value do not completely agree with the observed effective cross section due to some unknown reasons. We, however, try to obtain the fraction of real muons in these MC events by looking at OBSP information for which systematics would be canceled to some extent. The real-muon contamination is due to $Z \to \mu\mu$ events and the small peak around Z mass regions are completely attributed to them as expected. Regarding this, we comment that Z mass regions will be eventually excluded from the final analysis, which provides us a certain safety factor against the problem of real-muon contamination. Real-muon fractions, f, as a function of invariant mass are estimated, and a correction for real-muon contamination in the observed OS μ + hadronic tracks can be done by multiplying $1 - f$. The result is not statistically powerful, but there seem to still remain indications of the charge correlation in the data which are as much as a factor of 2 in a mass region around 40–50 GeV/c^2. The MC predictions obtained by explicitly rejecting real-muons using OBSP information are also included in the figure. It shows a similar level of charge correlation, and further says that the correlation is originating from W events, not from $Z \to \mu\mu$ events. The $Z \to \tau\tau$ strongly favors the OS combination as expected but the contribution itself is relatively small compared to the W events, thus the net effect is driven by the W events. From these investigation, we think that there may be charge correlations between leptons and additional track objects, thus the estimation of the fake-lepton backgrounds in the OS dilepton events using LS combinations is not necessarily ensured to lead to a correct answer. We can also say that the charge correlation may depend on the selection and on the kinematical space that we look at, and not always important especially when W events are not contributing much. For example, it might be reasonable to use LS combinations in the Z mass window. In general, we must always bear this in our mind when we analyze the OS dilepton events.

6 Bayesian Method

6.1 Bayes' Theorem

The probability that X will take the value x_i and Y will take the value y_j is written $p(X = x_i, Y = y_j)$ and is called *joint* probability of $X = x_i$ and $Y = y_j$. It is given by the number of points falling in the cell i, j as a fraction of the total number of points,and hence

$$p(X = x_i, Y = y_j) = \frac{n_{ij}}{N} \tag{6.1}$$

$$p(X = x_{ij}) = \frac{c_i}{N} \tag{6.2}$$

where $c_i = \sum_j n_{ij}$ so

$$p(X = x_i) = \sum_{j=1}^{L} p(X = x_i, Y = y_j) \tag{6.3}$$

Which is the sum rule of probability. The $p(X = x_i)$is called the *marginal* probability. If we consider only those instances for which $X = x_i$,then the fraction of such instance for which $Y = y_j$ is written $p(Y =_j |X = x_i)$ and is called the *conditional* probability of $Y = y_j$ given $X = x_i$. It is obtained by finding the fraction of those points in column i that fall in cell i, j and hence is given by

$$p(Y = y_j|X = x_i) = \frac{n_{ij}}{c_i} \tag{6.4}$$

so

$$\begin{aligned} p(X = x_i, Y = y_j) &= \frac{n_{ij}}{N}\frac{n_{ij}}{c_i}\frac{c_i}{N} \\ &= p(Y = y_j|X = x_i)p(X = x_i) \end{aligned} \tag{6.5}$$

Which is the product rule of probability.
From product rule ,together with the symmetry property $p(X, Y) = p(Y, X)$, we immediately obtain the following relation ship between conditional probabilities

$$p(Y|X) = \frac{p(X|Y)p(x)}{p(x)} \tag{6.6}$$

which is called Bayes' theorem.

$$\textbf{sum rule} : p(X) = \sum_Y p(X, Y) \tag{6.7}$$

$$\textbf{product rule} : p(X, Y) = p(Y|X)p(X) \tag{6.8}$$

Using the sum rule ,the denominator in Bayes' theorem can be expressed in term of quantities appearing in the numerator

$$p(X) = \sum_{Y} p(X|Y)p(Y) \tag{6.9}$$

6.2 Bayesian Probabilities

The Bayesian view, in which probabilities provide a quantification of uncertainty. Bayes' theorem was used to convert a probability into a posterior probability by incorporating the evidence provided by the observed data. For example, we capture our assumptions about $\boldsymbol{w}$, before observing the data $\mathcal{D} = \{t_1, \cdots, t_N\}$ is expressed through the condition probabilities $p(\mathcal{D}|\boldsymbol{w})$, the Bayes' theorem takes the following form

$$p(\boldsymbol{w}|\mathcal{D}) = \frac{p(\mathcal{D}|\boldsymbol{w})p(\boldsymbol{w})}{p(\mathcal{D})} \tag{6.10}$$

then allows us to evaluate the uncertainty in $\boldsymbol{w}$ *after* we have observed $\mathcal{D}$ in the form of the posterior probability $p(\boldsymbol{w}|\mathcal{D})$. The quantity $p(\mathcal{D}|\boldsymbol{w})$ on the right-handed side of Bayes'theorem is evaluated for the observed data set $\mathcal{D}$ and can be viewed as a function of the parameter vector $\boldsymbol{w}$, in which case it is called the *likelihood function.* It express how probable the observed data set is for different settings of the parameter vector $\boldsymbol{w}$. Note that the likelihood is not a probability distribution over $\boldsymbol{w}$, and its integral with respect to $\boldsymbol{w}$ does not (necessary) equal one. Given this definition of likelihood, we can state Bayes'theorem in words

$$\textit{posterior} \propto \textit{likelihood} \times \textit{prior} \tag{6.11}$$

where all of these quantities are viewed as functions of $\boldsymbol{w}$. The denominator is the normalization constant, which ensure that the posterior distribution on the left-hand side is a valid probability density and integrate to one. Indeed integrating both side of 7.5 with respect to $\boldsymbol{w}$, we can express the denominator in Bayes'theorem in term of the prior distribution and the likelihood function

$$p(\mathcal{D}) = \int p(\mathcal{D}|\boldsymbol{w})p(\mathcal{D})\, d\boldsymbol{w}. \tag{6.12}$$

In both the Bayesian and frequentist paradigms, the likelihood function $p(\mathcal{D}|\boldsymbol{w})$ plays a central role. However, the manner in which it is used is fundamentally different in the two approaches. In frequentist setting,$\boldsymbol{w}$ is considered to be a fixed parameter, whose value is determined by some form of 'estimator', and error bars on this estimate are obtained by considering in the distribution of possible data set $\mathcal{D}$(namely the one that is actually observed), and the uncertainty in the parameters is expressed through a probability distribution over $\boldsymbol{w}$.

A widely used frequentist estimator is maximum likelihood, in which $\boldsymbol{w}$ is set to the value that maximizes the likelihood function $p(\mathcal{D}|\boldsymbol{w})$. This corresponds to choosing the value of $\boldsymbol{w}$ for which the probability of the observed data set is maximized.

One advantage of the Bayesian viewpoint is that the inclusion of prior knowledge arises naturally. Suppose ,for instance, that a fair-looking coin is tossed three times and lands heads each time. A classical maximum likelihood estimate of the probability of landing heads would give 1, implying that all future tosses will land heads. By contrast, a Bayesian approach with any reasonable prior will lead to much less extreme conclusion

There has been much controversy and debate associated with the relative merits of the frequentist and Bayesian paradigms, which have not been helped by the fact that there is no unique frequentist, or even Bayesian, viewpoint. For instance, one common criticism of the Bayesian approach is that the prior distribution is often selected on the bias of mathematical convenience rather than as a reflection of any prior beliefs. Even the subjective nature of the conclusions through their dependence on the choice of prior is seen by some as a source of difficulty. Reducing the dependence on the prior is one motivation for so-called noninformative priors. However, these lead to difficulties when comparing different models, and indeed Bayesian methods based on poor choices of prior can give poor results with high confidence. Frequentist evaluation methods offer some protection from such problems, and techniques such as cross-validation remain useful in area such as model comparison.

7 Cross-Section

S

7.1 Measurement

7.1.1 Multivariate Analysis

Multivariate analysis is introduced for signal and background event separation from statistics and computer sciences. The Boosted decision trees are one of machine learning, which extends a simple cut-based analysis into a multivariate algorithm with a continuous discriminant output. Boosting is a process that can be used on any weak classifier and enhance separation of signal and background. The method contained in a computer package named T-MultiVariableAnalyser (TMVA) were used to increase the signal to background separation over more traditional cut based analyses. TMVA is packaged with the ROOT program from version 5.00 onwards, and implements a range of multivariable discrimination techniques which can be compared to find the best techniques foe the data. When using TMVA, the training and testing were performed within a ROOT macro environment; the implementation of the TMVA weights in the analysis was performed in stand-alone code fully compiled outside of root, but using libraries. **The Boosted Decision Trees** method creates a series of decision trees. Each of these is a random sequence of cuts placed on the input variables, with each new variable's cut varying depending on whether the event passed the previous cut or not. This creates per tree a random set of bins which are independent and contain different proportions of signal and background. An overall likelihood test is performed on all the bins created by a number of such decision trees called a forest. To optimize this forest, poorly-discriminating trees are removed or pruned Boosting refers to weighting the events in importance such that trees which separate difficult events are kept.

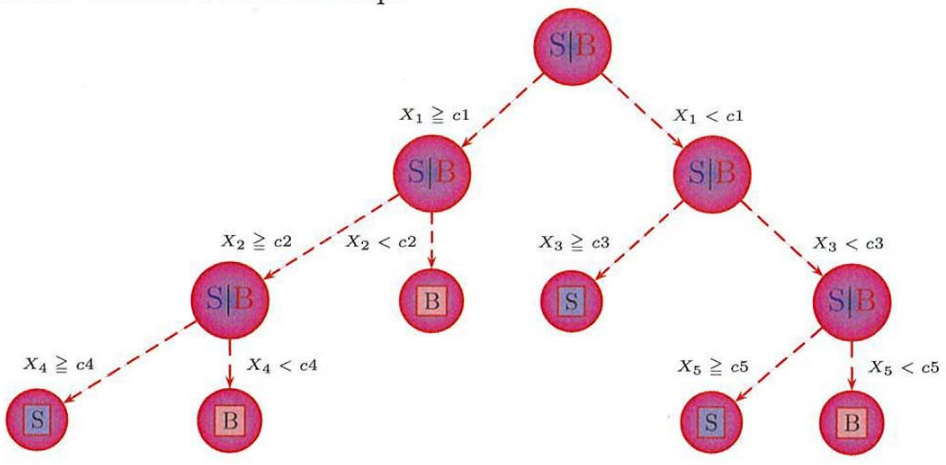

A schematic diagram of the Boosted Decision Trees

7.1.2 Decision Trees

A decision trees classifies events based on a set of cumulative selection criteria that define several disjoint subsets of events, each with a different signal purity. The decision trees is

built by creating two branches at every nonterminal node,splitting the sample of events under consideration into two subsets based on the most discriminating selection criterion for that sample. Terminal nodes are called leaves and each leaf has an assigned purity value p. A sample decision tree is illustrated in figure. An events defined by variables $\boldsymbol{x}$ will follow a unique path through the decision tree and end up in leaf. The associated purity p of the this leaf is the decision tree discriminant output for the events one of the primary advantages of decision trees over a cut-based analysis is that events which fail an individual cut continue to be considered by the algorithm. Limitations of decision trees include the probability of the tree structure with respect to the training sample composition, and the piecewise nature of the output. Training on different samples may produce very different trees with similar separation power. The discrete output comes from the fact that the only possible values are the purities of each leaf and the number of leaves is finite. Decision tree have interesting features,as follows: the tree has a human-readable structure, making it possible to know why a particular event was labeled signal or background; training is fast compared to neural network;decision trees can use discrete variables directly; and no preprocessing of input variables is necessary. In addition, decision are relatively insensitive to extra variables that are not powerful discriminators does not degrade the performance of the decision tree.

Decision Trees

- Assume the events are weighted with each event having weighW_i

  Define the purity of the sample in a node by

$$P = \frac{\sum_s W_s}{\sum_s W_s + \sum_b W_b} \tag{7.1}$$

  where $\sum_s$ is the sum over signal and events and $\sum_b$ is the sum over background events.

- Note that $P(1-P)$ is 0 if the sample is pure signal or pure background. For a given node let

$$\text{Gini} = \sum_{i=1}^{n} P(1-P) \tag{7.2}$$

  where n is the number of events on the node

- The criterion chosen is to minimize

$$\text{Gini}_{\text{child,left}} + \text{Gini}_{\text{child,right}}. \tag{7.3}$$

- To find the split that maximizes the overall tree purity

$$\text{Criterion} = \text{Gini}_{\text{mother}} - \text{Gini}_{\text{child,left}} - \text{Gini}_{\text{child,right}}. \tag{7.4}$$

  At the end, if a leaf has purity greater than $\frac{1}{2}$, then it is called a signal leaf, otherwise , a background leaf. Events are c classified signal have score of 1 if they land on a signal leaf and background have score of -1 if they land on a background leaf. The resulting tree is a decision tree.

7.1.3 Boosting

Boosting is a powerful technique for combining multiple 'base' classifiers to produce a form of committee whose performance can be significantly better than that of any of the base classifiers. Here we describe the most widely used form of boosting algorism called E_TAdaBoost, short for 'adaptive boosting',developed by Freund and Schapire. Boosting can give good results even if the base classifiers have a performance that is only slightly better than random, and hence sometimes the base classifiers are known weak learners. Originally designed for solving classification problems, boosting can also be extended to regression . The principal difference between boosting and the committee method such as bagging discussed above, is that the base classifiers are trained in sequence, and each base classifier is trained using a weighted form of the data set in which the wighting coefficient associated with each data point depend on the performance of the previous classifiers. In particular, points that are misclassified by one of the base classifiers are given greater weight when used to train the next classifier in the sequence. Once all the classifiers have been trained, as illustrated schematically in figure.

Consider a two class classification problem, in which the training data comprises input vectors $\boldsymbol{x_1}, \cdots, \boldsymbol{x_N}$ along with corresponding binary target variables $t_1, \cdots, t_N$ where $t_n \in \{-1, 1\}$. Each data point is given an associated weighting parameterw_n, which is initially set $\frac{1}{N}$ for all data points. We shall suppose that we have a procedure available for training a base classifier using weighted data to give a function $y(\boldsymbol{x}) \in \{-1, 1\}$. At each stage of the algorism, AdaBoost trains a new classified data set in which the weighting coefficients are adjusted according to the performance of the previously trained classifier so as to give greater weight to the misclassified data points. Finally, when the desired number of base classifiers have been trained, they are combined to form a committee using coefficients that give different weight to different base classifiers. The precise form of the AdaBoost algorism is given below.

7.1.4 AdaBoost

- Initialize the data weighting coefficient $\{w_n\}$ by setting $w_n = \frac{1}{N}$ for $n = 1, \cdots, N$
- For $m = 1, \cdots, M$:
  - Fit a classifier $y_m(\boldsymbol{x})$ to the training the data by minimizing the weighed error function

$$J_m = \sum_{n=1}^{N} w_n^{(m)} I(y_m(\boldsymbol{x}) \neq t_n) \tag{7.5}$$

    where $I(y_m(\boldsymbol{x}) \neq t_n)$ is the indicator function and equal 1 when $\boldsymbol{x}) \neq t_n$ and 0 otherwise.

  - Evaluate the quantities

$$\epsilon_m = \frac{J_m = \sum_{n=1}^{N} w_n^{(m)} I(y_m(\boldsymbol{x}) \neq t_n)}{\sum_{n=1}^{N} w_n^{(m)}} \tag{7.6}$$

    and then use these to evaluate

$$\alpha_m = \ln \frac{1 - \epsilon_m}{\epsilon_m}. \tag{7.7}$$

– Update the data weighting coefficients

$$w_n^{(m+1)} = w_n^{(m)} \exp\{\alpha_m I(y_m(\boldsymbol{x}) \neq t_n)\} \tag{7.8}$$

– Make predictions using the final model, which is given by

$$Y_M(\boldsymbol{x}) = \text{sign}\left[\sum_{m=1}^{M} \alpha_m y_m(\boldsymbol{x})\right] \tag{7.9}$$

We see that the first base classifier $y_1(x)$ is trained using weighting coefficient $w_n^{(1)}$ that all equal, which therefor corresponds to the usual procedure for training a single classier. From 7.8, we see that in subsequent iterations the weighting coefficient $w_n^{(m)}$ are increased for data points that are misclassied and unchanged for data points that are correctly classified. misclassified classifiers are therefore forced to place greater emphasis on points that have been misclassified by previous classifiers receive ever greater weight. The quantities ϵ_m represent weighted measures of the error rate each of the base classifiers on the data set. We therefor see that the weighting coefficients α_m defined by 7.7 give greater weight to the more accurate classifiers when computing the overall output given by 7.9.

7.1.5 Input variable

The BDT is insensitive to including input variables with low separation powers, because the pruning procedure remove the splitting nodes under such variables, while the other multivariate techniques have to carefully select the input variables and deal with it, for example Artificial Neural Network. If a strongly correlated variables is selected as input variable, the performance should not be always good. We have selected 8 kinematics to be used the input variables to construct BDT discriminant.

- 1st lepton p_T
- 2nd lepton p_T
- Missing E_T
- Dilepton Mass
- MetSpec

  $\not\!\!E_T$ if $\Delta\phi(\not\!\!E_T$, ℓ or jet) $> \frac{\pi}{2}$ or
  $\not\!\!E_T \sin(\Delta\phi(\not\!\!E_T$, ℓ or jet)) if $\Delta\phi(\not\!\!E_T$, ℓ or jet) $< \frac{\pi}{2}$

- H_T (Sum of 1st, 2nd lepton p_T, jets E_T(E_T >15 GeV and $|\eta|$ <2.0), and $\not\!\!E_T$)
- Number of Jets with E_T >15.0 GeV

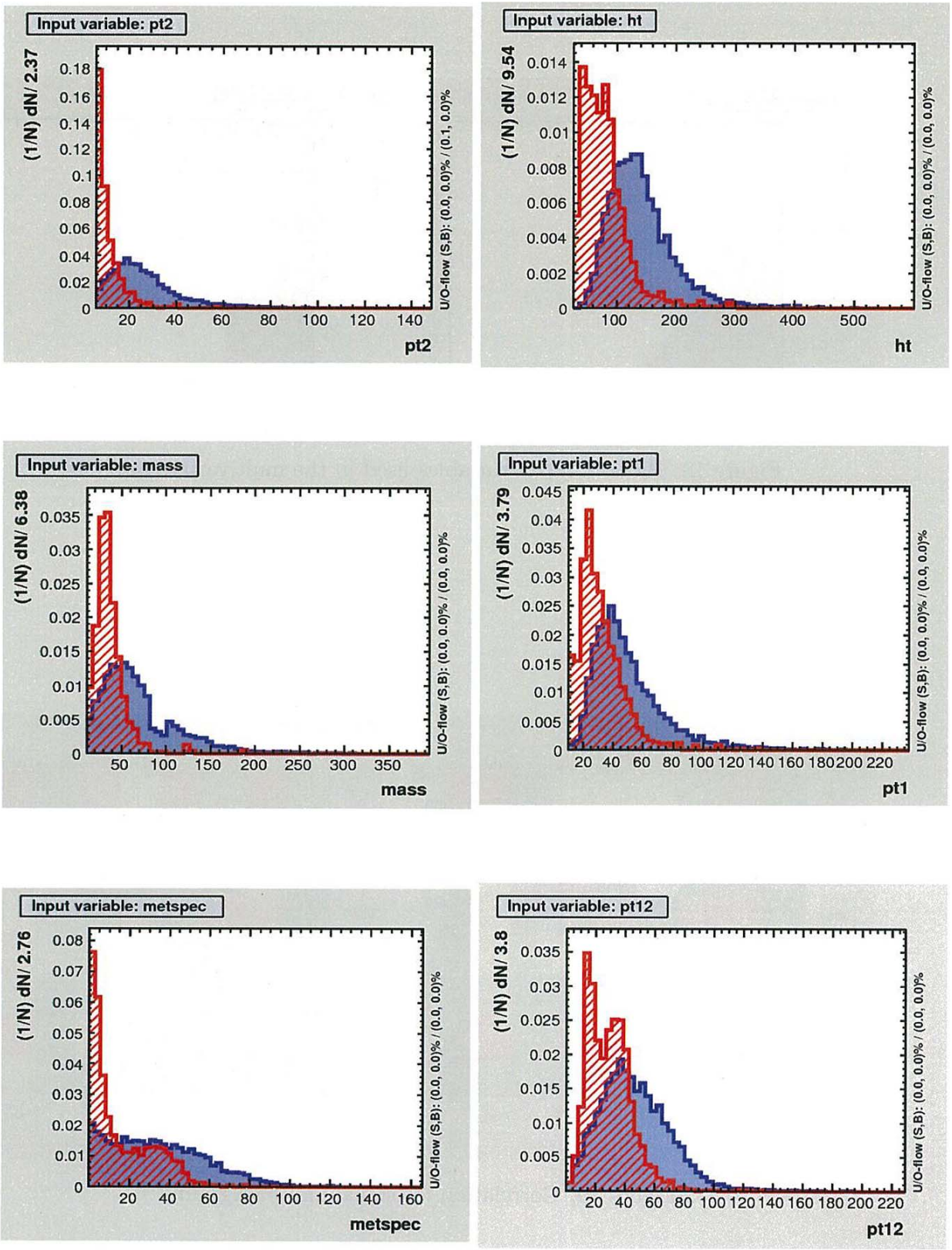

Figure 17: Plots of input variables used in the multivariate analysis.

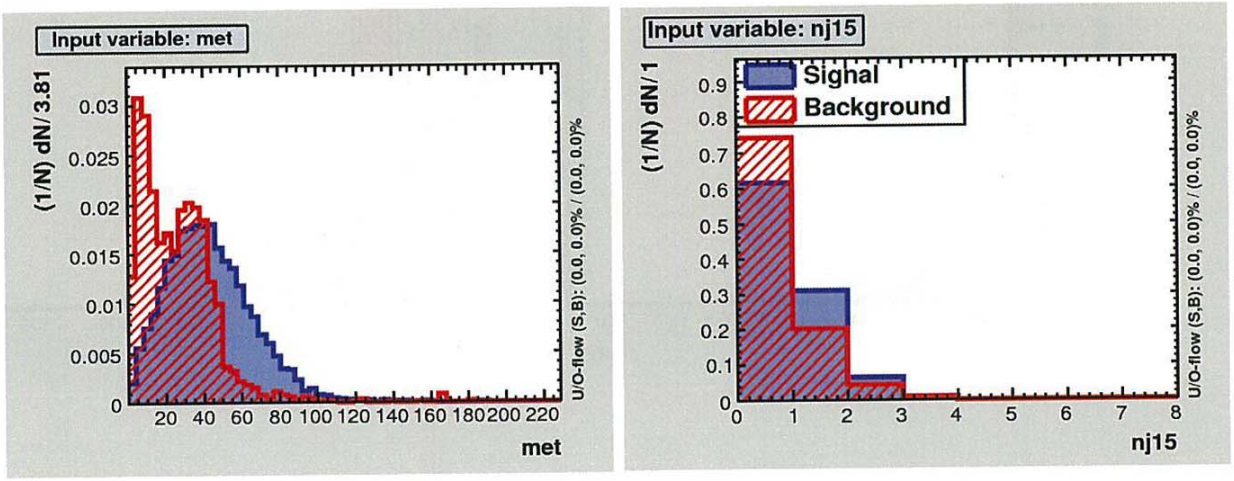

Figure 18: Plots of input variables used in the multivariate analysis.

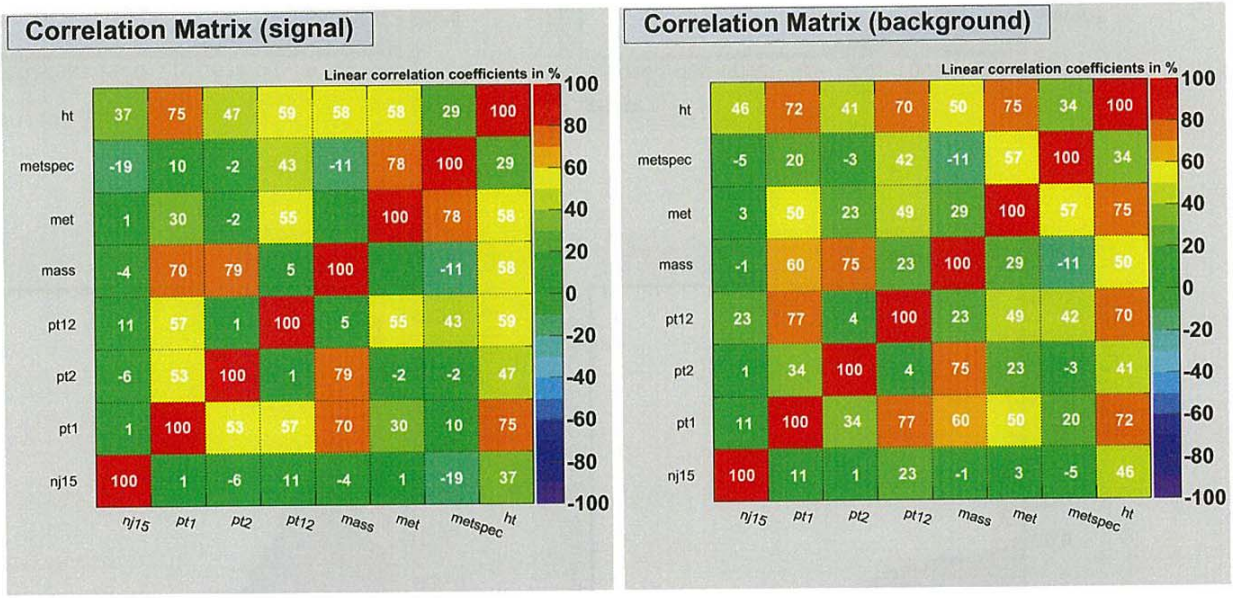

Figure 19: Correlation for signal and background

Rank	Variable
1	p_{T2}
2	H_T
3	Mass
4	p_{T1}
5	Metspec
6	p_{T12}
7	Met
8	N_{j15}

Table 10: Ranking input variables, ranking result (top variable is best ranked)

7.1.6 BDT output plots

Discriminant output shapes for signal and background are shown in following fig.

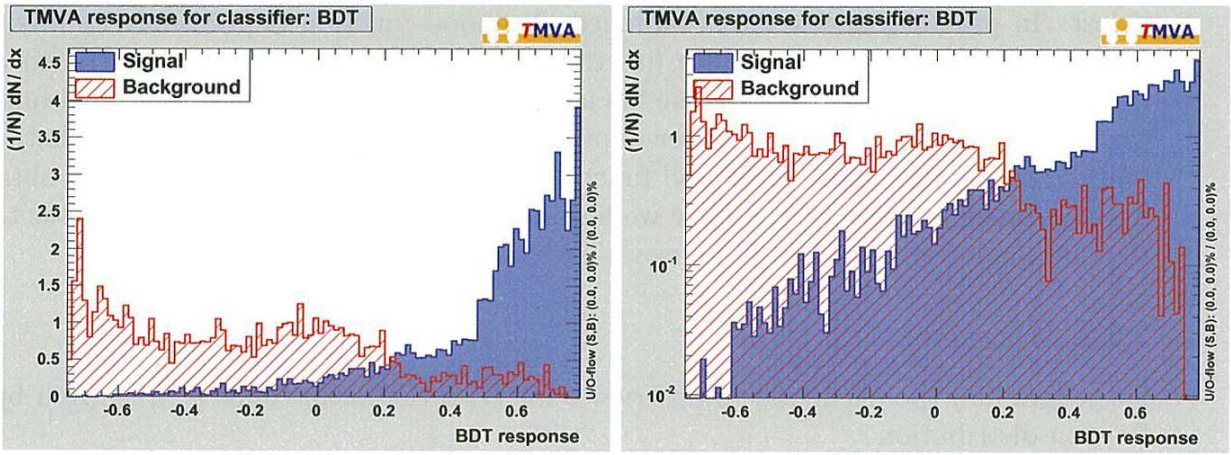

Figure 20: Fake background and WZ signal separation plots for training plots (linear and log)

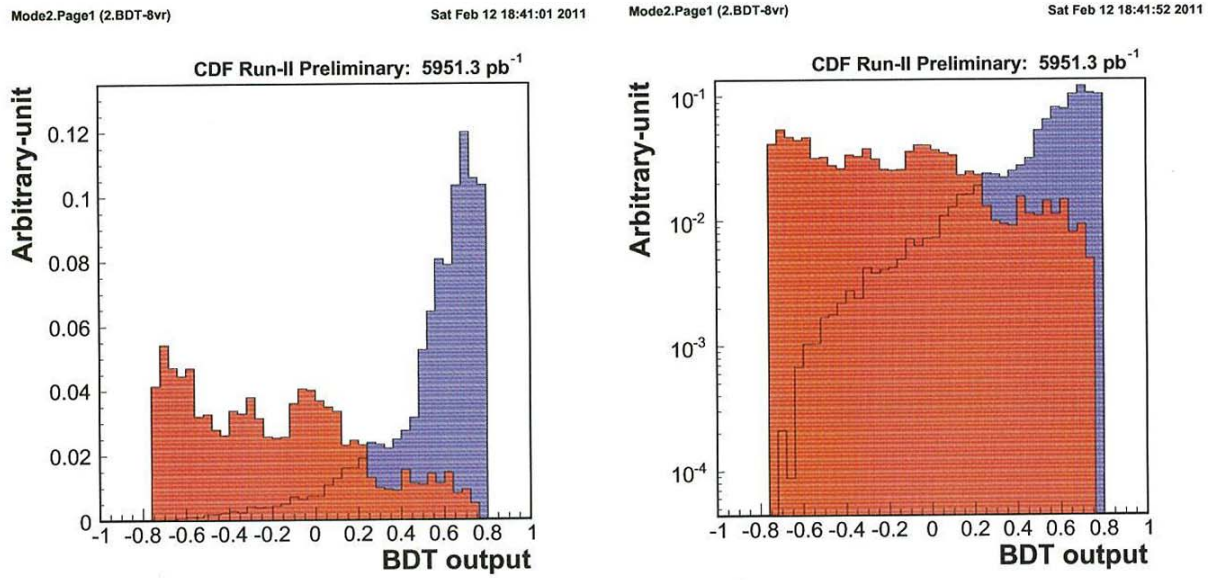

Figure 21: Fake background and WZ signal separation plots for test plots (linear and log)

7.2 Cross Section Measurement

We use approach to extract the cross section σ from the observed binned discriminant distributions. In principle, the binning of the data should be avoided because information is lost. In practice, however, an unbinned likelihood function is invariably approximate because of the need to fit smooth functions to the distributions of the unbinned data. Consequently, the uncertainty in the fits induces an uncertainty in the likelihood function that grows linearly with the number of events. Without study, it is not clear whether an binned, but approximate, likelihood function will yield superior results to those obtained from a binned but exact one. Since we have not yet studied the matter, we choose to bin the data and avail ourselves of an exact likelihood function.

7.2.1 Bayesian

For a give bin, the likelihood to observe count D, if the mean count is d, is given by the Poisson distribution

$$L(D|d) = \frac{\exp(-d)d^D}{D!} \tag{7.10}$$

The mean count d is the sum of the predicted contributions from the signal and background sources

$$\begin{aligned} d &= \text{signal} + \text{background} \\ &= \alpha\mathcal{L}\sigma + b \\ &= a\sigma + b \end{aligned} \tag{7.11}$$

where α is the signal acceptance, $\mathcal{L}$ the integrated luminosity, σ the WZ production cross section, b the mean count for background source. and $a \equiv \alpha\mathcal{L}$ is the effective luminosity

for the signal. For a distribution of observed counts, the single-bin likelihood is replaced by a product likelihoods

$$L(\boldsymbol{D}|\boldsymbol{d}) \equiv L(\boldsymbol{D}|\sigma, \boldsymbol{a}, \boldsymbol{b}) = \prod_{i=1}^{N} L(D_i|d_i) \tag{7.12}$$

where $\boldsymbol{D}$ and $\boldsymbol{d}$ represent vectors of the observed and mean counts, and $\boldsymbol{a}$ and $\boldsymbol{b}$ are vectors of effective luminosity and background yield. The product is over N statistically independent bins: all bins of combination of these channels.

$$L(\boldsymbol{D}|\boldsymbol{d}) = \prod_{i=1}^{N} \frac{\exp\left(-(a_i\sigma + b_i)\right)(a_i\sigma + b_i)^{n_i}}{n_i!} \tag{7.13}$$

From Bayes' theorem, we can compute the posterior probability density of the parameters $p(\sigma, \boldsymbol{a}, \boldsymbol{b}|\boldsymbol{D})$, which is then integrated with respect to the parameters $\boldsymbol{a}$ and $\boldsymbol{b}$ to obtain the posterior density for the WZ production cross section, given the observed distribution of counts $\boldsymbol{D}$,

$$p(\sigma|\boldsymbol{D}) = \frac{1}{\mathcal{N}} \iint L(\boldsymbol{D}|\sigma, \boldsymbol{a}, \boldsymbol{b})\, d\boldsymbol{a} d\boldsymbol{b}. \tag{7.14}$$

Here, $\mathcal{L}$ is an overall normalization obtained from the requirement

$$\int p(\sigma|\boldsymbol{D})\, d\sigma = 1 \tag{7.15}$$

where the integration is performed numerically up to an upper bound σ_{max} when the value of the posterior is sufficiently close to zero. The function $\pi(\sigma, \boldsymbol{a}, \boldsymbol{b})$ is the prior probability density, which encodes our knowledge of the parameters $\sigma, \boldsymbol{a}$ and $\boldsymbol{b}$. Since our knowledge of the cross section σ does not inform our prior knowledge of $\boldsymbol{a}$ and $\boldsymbol{b}$, we write the prior density as

$$\pi(\sigma, \boldsymbol{a}, \boldsymbol{b}) = \pi(\boldsymbol{a}, \boldsymbol{b})\pi(\sigma) \tag{7.16}$$

The prior density for the cross section is taken to be a nonnegative flat prior,

$$\pi(\sigma) = \frac{1}{\sigma_{max}} \tag{7.17}$$

for $\sigma \geqq 0, \pi(\sigma) = 0$ otherwise. We make this choice because it is simple to implement.

$$p(\sigma|\boldsymbol{D}) = \frac{1}{\mathcal{N}\sigma_{max}} \iint L(\boldsymbol{D}|\sigma, \boldsymbol{a}, \boldsymbol{b})\pi(\boldsymbol{a}, \boldsymbol{b})\, d\boldsymbol{a} d\boldsymbol{b} \tag{7.18}$$

We take the mode of $p(\sigma|\boldsymbol{D})$ as our measure of the cross section, and the 68% interval about the mode as our measure of the uncertainty with the cross section is measured. We have verified that these intervals, although Bayesian, have approximately 68% coverage probability and can therefor be interpreted as approximate frequentist intervals if desired. The integral in 7.18 is done numerically using Mote Carlo importance sampling. We

generate a large number K of points $(\boldsymbol{a}_k, b_k)$ randomly sampled from the prior density $\pi(\boldsymbol{a}, \boldsymbol{b})$ and estimate the posterior density using

$$\begin{aligned} p(\sigma|\boldsymbol{D}) &\propto \iint L(\boldsymbol{D}|\sigma, \boldsymbol{a}, \boldsymbol{b}) \\ &\approx \frac{1}{K}\sum_{k=1}^{K} L(\boldsymbol{D}|\sigma, \boldsymbol{a_k}, \boldsymbol{b_k}) \end{aligned} \tag{7.19}$$

In the presence of signals, we use the same procedure and calculate the posterior probability density according to 7.19, replacing σ by σ_{WZ}

7.2.2 Expected WZ Cross Section

We measure the expected WZ production cross section for the various channels by setting the number of the data events in each channel equal to the expected number of background events plus the expected number of signal events.

At first, as compared with BDT we calculate the production cross section using the distribution of the 2nd lepton p_T whose variable is best ranked in signal and background separation with BDT. And next, we calculate WZ cross section using the BDT (Multivariate analysis). We obtain the following results:

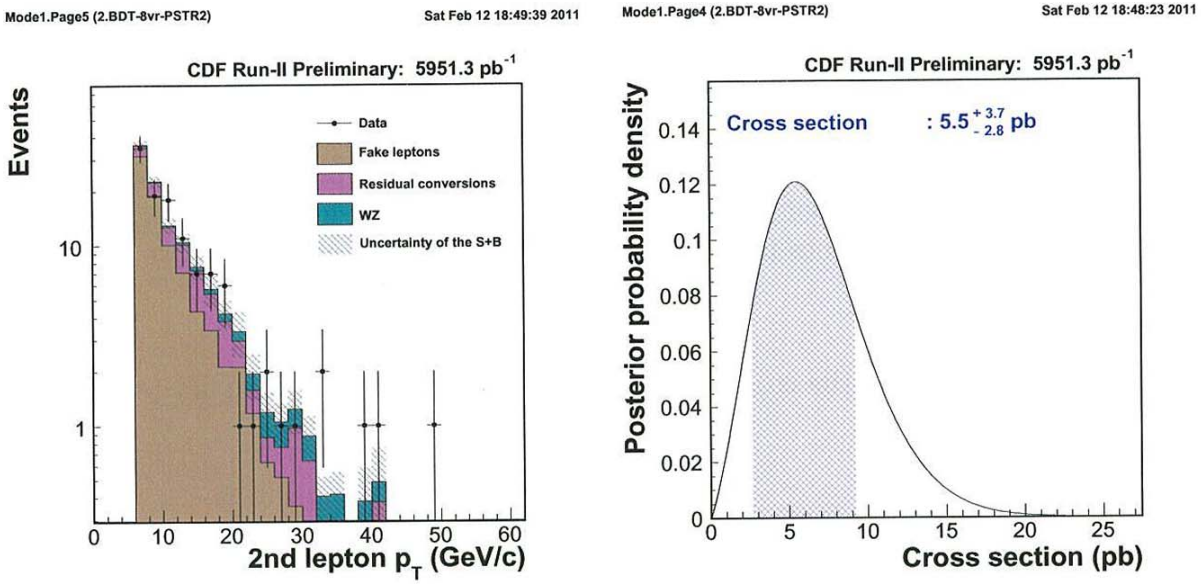

Figure 22: 2nd lepton p_T distribution and the WZ cross section posterior

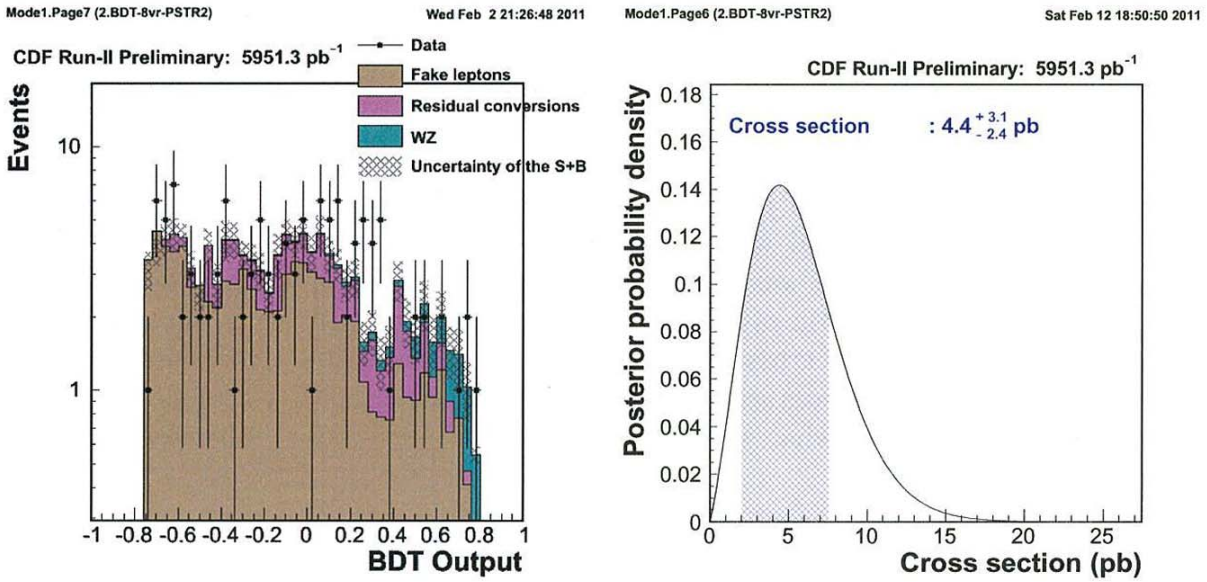

Figure 23: BDT output and the WZ cross section posterior

$$\begin{aligned}\sigma_{WZ} &= 5.5^{+3.7}_{-2.8}(\text{2nd lepton } p_T) \\ &= 4.4^{+3.1}_{-2.4}(\text{BDT})\end{aligned} \tag{7.20}$$

The expected production cross section agree with the standard model cross section (3.65 pb) and consistent with the SM. WZ cross section using the BDT is better than that not using it.

8 Conclusion

The Boosted Decision Trees was used to discriminate the WZ signal from the background, and a Bayesian approach was used when obtaining the WZ production cross section. The expected WZ production cross section was $5.5^{+3.7}_{-2.8}$ pb^{-1} when we calculated it from the distribution of 2nd lepton p_T. The WZ cross section which predicted by the standard model is 3.65 pb^{-1}. And when we used the multivariate analysis BDT, the expected production cross section was $4.4^{+3.1}_{-2.4}$ pb^{-1}. The both results which were derived by the distribution of 2nd lepton p_T and BDT output are consistent with the standard model. Also the results of WZ cross section using the BDT is better than that of not using it. Since WZ production cross section in the SM depends on the WWZ triple gauge coupling, we surely can also say what we have confirmed the gauge boson self-interaction.

References

[1] Halzen-Martin"Quarks-and-Leptons-Introductory-Course-in-Modern-Particle-Physics"

[2] F.MANDL G.SHAW "QUANTUM FIELD THEORY"

[3] D. Hidas, *et al.*, Search for $H- > WW$ Production Using Combined ME and NN Method in 1.9fb^{-1}, CDF note no. 9163.

[4] T. Junk, "Sensitivity, Exclusion, and Discovery with Small Signals, Large Backgrounds, and Large Systematics," CDF 8128.

[5] J.G. Heinrich, "The Log Likelihood Ratio of the Poisson Distribution for Small μ", CDF note 5718, version 2.

[6] Joel Heinrich et al., Interval estimation in the presence of nuisance parameters. 1. Bayesian approach., CDF Internal Note 7117, (2004).

[7] John Conway "Calculation of Cross Section Upper Limits Combining Channels Incorporating Correlated and Uncorrelated Systematic Uncertainties", CDF/PUB/STATISTICS/PUBLIC/6428.

[8] Joel Heinrich "A Bayes Factor Example : Poisson Discovery' , CDF/MEMO/STATISTICS/PUBLIC/9678.

[9] L. DEMORTIER "DEALING WITH DATA: SIGNALS, BACKGROUNDS, AND STATISTICS".

[10] Luc Demortier "A Convolution Method for Folding Systematic Uncertainties into Likelihood Functions" , CDF/MEMO/STATISTICS/PUBLIC/5305 Version 1.00.

[11] Luc Demortier "Everything you always wanted to know aboutpulls" , CDF/ANAL/PUBLIC/5776 Version 2.10.

[12] Luc Demortier "Objective Bayesian Upper Limits for Poisson Processes" , CDF/MEMO/STATISTICS/PUBLIC/5928 Version 2.10.

[13] Joel Heinricha, Craig Blockerb, John Conwayc, Luc Demortierd, Louis Lyonse, Giovanni Punzif , Pekka K. Sinervog "Interval estimation in the presence of nuisance parameters. 1. Bayesian approach." , CDF/MEMO/STATISTICS/PUBLIC/7117.

[14] The CDF Collaboration "Measurement of WW production cross section in $p\bar{p}$ collisions $\sqrt{s}$=1.96 TeV using 3.6 fb^{-1} CDF Run II Data ".

[15] Toru Okusawa, Yoshihiro Seiya, Takayuki Wakisaka, and Kazuhiro Yamamoto "Baseline Selection of High-pT Dilepton Events to Search for the Wh Production" , CDF/ANAL/EXOTIC/CDFR/7260 Version 3.0.

[16] Toru Okusawa, Yoshihiro Seiya, Takayuki Wakisaka, and Kazuhiro Yamamoto "Estimation of Monte-Carlo Scale Factors for the High-p_T Like-Sign Dilepton Analysis to Search for the Wh Production" , CDF/ANAL/EXOTIC/CDFR/9238. Version 3.0

[17] Toru Okusawa, Yoshihiro Seiya, Takayuki Wakisaka, and Kazuhiro Yamamoto "Study of Fake-Lepton Rates for the High-p_T Like-Sign Dilepton Analysis to Search for the Wh Production" , CDF/ANAL/EXOTIC/CDFR/9239 Version 2.0.

[18] Toru Okusawa, Yoshihiro Seiya, Takayuki Wakisaka, and Kazuhiro Yamamoto "Study of Conversion Detection Efficiency for the High-p_T Like-Sign Dilepton Analysis to Search for the W h Production" , CDF/ANAL/EXOTIC/CDFR/8078 Version 2.0.

[19] Alberto Annovil, Viviana Cavaliere, Maria Agnese Ciocci, Januscia Duchini, Paolo Mastrandrea, Marco Rescigno, Anna Sfyrla "Search for Diboson production in $WW\not{W}Z \to \nu jj$ using 3.9 fb^{-1}".

[20] D0 Collaboration "Evidence for production of single top quarks" ,arxiv.org/abs/0803.0739v2.

[21] Hai-Jun Yanga , Byron P. Roea , Ji Zhub "Studies of Boosted Decision Trees for MiniBooNE Particle Identification" , arxiv.org/abs/physics/0508045v1.

[22] Etienne Grossmann "A Theory of Probabilistic Boosting, Decision Trees and Matryoshki" , arxiv.org/abs/cs/0607110v1.

[23] Byron P. Roe, Hai-Jun Yang, Ji Zhu, Yong Liu, Ion Stancu, Gordon McGregor "Boosted Decision Trees as an Alternative to Artificial Neural Networks for Particle Identification" , arxiv.org/abs/physics/0408124v2.

[24] M. Dobbs, M. Lefebvre "Unweighted event generation in hadronic WZ production at order(α_S)" , arxiv.org/abs/hep-ph/0011206v1.

[25] Elena Accomando, Ansgar Denner, Stefano Pozzorini "Electroweak-correction effects in gauge-boson pair production at the LHC" , arxiv.org/abs/hep-ph/0110114v2.

[26] E. Accomando, A. Kaiser "Electroweak corrections and anomalous triple gauge-boson couplings in WW and WZ production at the LHC" , arxiv.org/abs/hep-ph/0511088v1.

[27] E. Accomando "Pseudo-observables in Axial gauge" , arxiv.org/abs/hep-ph/0604273v1.

[28] H. Aihara, T. Barklow, U. Baur, J. Busenitz, S. Errede, T. A. Fuess, T. Han, D. London, J. Ohnemus, R. Szalapski, C. Wendt, and D. Zeppenfeld , "ANOMALOUS GAUGE BOSON INTERACTIONS " , arxiv.org/abs/hep-ph/9503425v1

[29] Matthew Dobbs "Probing the Three Gauge-boson Couplings in 14 TeV Proton-Proton Collisions" , A Dissertation Submitted in Partial Fulfillment of the Requirements for the Degree of DOCTOR OF PHILOSOPHY in the Department of Physics and Astronomy, University of Victoria.

[30] Konstantinos Bachas, Tom Barber, Richard Batley, Andrea Bocci, Ilectra Christidi, Tiesheng Dai, Al Goshaw, Liang Han, Chris Hays, Suen Hou, Yi Jiang, Ashutosh Kotwal, Mark Kruse, Dan Levin, Xuefei Li, Zhijun Liang, Hong Ma, Chara Petridou, Dragan Popovic Dusan Reljic, Dimos Sampsonidis, Ljiliana Simic, Nenad Vranjes, Song-Ming Wang, Pat Ward, Alan Wilson, Haijun Yang, Yi Yang, Pei Zhang, Zhengguo Zhao, Jia "ATLAS CSC NOTE Diboson Physics Studies With the ATLAS Detector (Long version of the public diboson CSC note)".